A&A 425, 443–456 (2004)
DOI: 10.1051/0004-6361:20041058

Astronomy & Astrophysics

Multi-frequency study of extragalactic supernova remnants and H II regions

Sculptor group Sd galaxy NGC 300⋆

J. L. Payne[1], M. D. Filipović[2,3], T. G. Pannuti[4], P. A. Jones[3], N. Duric[5], G. L. White[1], and S. Carpano[6]

[1] Centre for Astronomy, James Cook University, Townsville, QLD, 4811, Australia
e-mail: snova4@msn.com
[2] University of Western Sydney, Locked Bag 1797, Penrith South, DC, NSW, 1797, Australia
[3] Australia Telescope National Facility, CSIRO, PO Box 76, Epping, NSW, 1710, Australia
[4] Spitzer Science Center, California Institute of Technology, Mailstop 220-6, Pasadena, CA 91125, USA
[5] Department of Physics and Astronomy, University of New Mexico, 800 Yale Bd. N.E., Albuquerque, NM 87131, USA
[6] Institut für Astronomie und Astrophysik, Universität Tübingen, Sand 1, 72076 Tübingen, Germany

Received 8 April 2004 / Accepted 4 June 2004

Abstract. We present a multi-frequency study of supernova remnants (SNRs) and H II regions in the nearby Sculptor Group Sd galaxy NGC 300, based on new ATCA observations at the wavelengths of 13 and 20 cm, *XMM-Newton* observations, newly-processed *ROSAT* (PSPC/HRI; Read & Pietsch 2001) and VLA (20/6 cm) images of this galaxy. We have investigated the physical properties at the X-ray and radio wavelengths of the 28 optical SNRs found by Blair & Long (1997) and have expanded on the multi-wavelength work by Pannuti et al. (2000) on this same galaxy. From a total of 54 radio sources and 11 X-ray sources, we report 18 SNRs and three (3) SNR candidates (classified by spectral index alone) in NGC 300. Five of these 18 SNRs are associated with reported optical SNRs and three have X-ray counterparts. An additional 12 radio SNRs are seen in the Blair & Long (1997) [S II] images. We also investigate the luminosity function of our SNRs. Three background radio sources are confirmed and 12 other sources could represent additional background objects. Twenty two radio correlations with OB associations within NGC 300 correspond to either H II regions or SNRs making them a good tracer of SNRs near star-forming regions. Additionally, two radio sources coincide with potential globular clusters of NGC 300 reported by Kim et al. (2002).

Key words. galaxies: individual: NGC 300 – ISM: supernova remnants – radio continuum: galaxies – X-rays: galaxies – ISM: H II regions

1. Introduction

Supernova remnants (SNRs) are associated with many crucial processes within galaxies, but a complete understanding of these sources remains elusive. While many SNRs located within the Milky Way Galaxy have been extensively studied (see for example, the recent multi-wavelength study of the Galactic SNR 3C 397; Dyer & Reynolds 1999), such work has been hampered by factors such as massive photoelectric absorption along the plane of the Galaxy at short wavelengths, as well as significant uncertainties in distances to SNRs (and corresponding diameter uncertainties). In addition, the position of the Sun within the Galactic disk and toward its edge makes it difficult to completely sample all of the Galactic SNRs.

To address these difficulties and to garner more insights into the nature of SNRs, observers have searched for SNRs in nearby galaxies such as the Large Magellanic Cloud (LMC) (Filipović et al., in preparation; Williams et al. 1999) , the Small Magellanic Cloud (SMC) (Filipović et al., in preparation), M 31 (Braun & Walterbos 1993), M 33 (Gordon et al. 1998), and the Sculptor Group galaxies NGC 300 and NGC 7793 (Blair & Long 1997, hereafter referred to as BL97; and Pannuti et al. 2002). Most of these surveys have concentrated on optical methods to detect SNRs and have met with considerable success in revealing a large number of new sources. However, such optical observations need to be complemented by observations at other wavelengths associated with emission from SNRs (such as X-ray and radio) to both detect a maximum number of SNRs in a galaxy of interest and to locate SNRs at all stages of their evolution.

⋆ Figures 8 and 9 are only available in electronic form at http://www.edpsciences.org

Table 1. Important properties of NGC 300. (NED = NASA/IPAC Extragalactic Database).

Property	Value (Reference)
Hubble type	SA(s)d (Tully 1988)
RA (J2000.0)	$00^h54^m53.48^s$ (NED)
Dec (J2000.0)	$-37°41'3.8''$ (NED)
Inclination	46 degrees (Tully 1988)
Distance	2.02 Mpc (Freedman et al. 2001)
Linear conversion	1 arcsec = 9.8 pc
Observed diameter D_{25}	20.2 arcmin (Tully 1988)
Mass (H I)	2.4×10^9 $M_\odot$ (Tully 1988)
N_H column density	2.97×10^{20} cm^{-2} (Read et al. 1997)
SNRs with optical flux	28 (Blair & Long 1997)
SNRs with radio flux	17 (Pannuti et al. 2000)
SNRs with X-ray flux	6 (Read & Pietsch 2001)

As pointed out in Lacey & Duric (2001), there may be a selection effect inherent in optical surveys, which are more sensitive to detecting SNRs away from H II regions. Such SNRs may be weak emitters in the X-ray and radio because of their location within low density environments which are not conducive to high X-ray and radio luminosities. In contrast, SNRs that are powerful sources of X-ray and radio emission are often located within H II regions. It is precisely because of their location in H II regions that they may be missed by optical surveys.

Although there are certainly exceptions, it can be thought that SNRs located in regions of low density were parented by low-mass white dwarf progenitor stars as Type Ia supernovae, while in contrast SNRs that are found in regions of high density were created by high-mass progenitor stars such as Type Ib/Ic/II supernovae. Thus, multi-wavelength studies also give a more complete picture of a galaxy's star formation history (Pannuti et al. 2002).

In this paper, we present results of a multi-wavelength search for SNRs in NGC 300 using new radio and X-ray data. Table 1 lists some of the more important properties of this galaxy. In Sect. 2, we describe our observations and data analysis. We discuss and explain the method used to identify SNRs, H II regions and background sources in Sect. 3. Position and flux density analysis is presented in Sect. 4, and a description of individual sources is given in Sect. 5. Finally, Sect. 6 is a summary and concluding discussion.

2. Observations and data analysis

2.1. Radio-continuum data

Radio-continuum observations of NGC 300 were made on 28 February 2000 with the Australia Telescope Compact Array (ATCA). The array was in the 6C antenna configuration, with baselines ranging between 153 and 6000 m. All observations were made simultaneously at 1374 and 2496 MHz (λ = 20 and 13 cm). Using this baseline configuration, we achieved a resolution of 6″ for each frequency (Table 2). This was considered as the best angular resolution with which to study NGC 300 in detail, ensuring at the same time sufficient sensitivity to any extended emission component. Primary flux density calibration was achieved using PKS 1934-638 and for phase calibration we used the secondary calibrator J0048-427. Data reductions were performed using the Multi-channel Image Reconstruction, Image Analysis and Display (MIRIAD) software package (Sault & Killeen 2003). Radio-continuum images of these observations are shown in Figs. 1 and 2.

Table 2. Summary of radio-continuum observations of the region of NGC 300.

Radio telescope	Freq. (MHz)	Beam size	rms Noise (mJy/b.a.)	Obs. date
ATCA	1374	$6'' \times 6''$	0.058	28 Feb. 2000
ATCA	2496	$6'' \times 6''$	0.062	28 Feb. 2000
VLA	1465	$4.70'' \times 3.76''$	0.066	13 June 1998
VLA	4885	$8.63'' \times 4.22''$	0.037	22 May 1993

NGC 300 was also observed by Pannuti et al. (2000) (hereafter referred to as PDL) using the Very Large Array (VLA) of the National Radio Astronomy Observatory (NRAO) at a wavelength of 6 cm in the hybrid CnB configuration (northern arm in the B array) on 22 May 1993 and at a wavelength of 20 cm in the BnA configuration on 13 June 1998 (Table 2). To minimize bandwidth smearing, which limits the field of view when observing in normal continuum mode, the VLA observed NGC 300 in multi-channel line mode with seven channels per IF and a channel width of 3.125 MHz, thereby synthesizing a total band of 37.5 MHz after dropping the first of the seven channels. The effective observing frequencies for the images made from the remaining six channels were 4860 MHz (6 cm) and 1448 MHz (20 cm). Data reduction were performed using the Astronomical Image Processing System (AIPS) software package (Greisen 2003).

The VLA images were corrected for primary beam attenuation and then converted to MIRIAD format before undertaking flux density measurements using the MIRIAD package. A summary of all radio observations is given in Table 2.

2.2. X-ray data

2.2.1. XMM-Newton

XMM-Newton observations on NGC 300 occurred December of 2000 and January of 2001 during revolutions 192 (~37 ks) and 195 (~47 ks), respectively. Data was collected using the EPIC MOS 1, MOS 2 and PN detectors utilizing a medium filter (Ehle et al. 2003). *XMM-Newton*'s 5σ sensitivity limit is estimated at $\sim 1.4 \times 10^{36}$ ergs s^{-1} (1 erg s^{-1} = 10^{-7} Watts).

After processing each dataset (using Science Analysis Software, SAS; Loiseau 2003), an X-ray image of NGC 300 was created (see Fig. 3). To do this, filtered MOS 1 event files from revolution 192 and 195 were first merged. In similar fashion, merged MOS 2 and PN event files from both observations were created. MOS 1 and MOS 2 merged event files were next combined and finally a single event file containing all events from both observations created the image. Editing provided "good

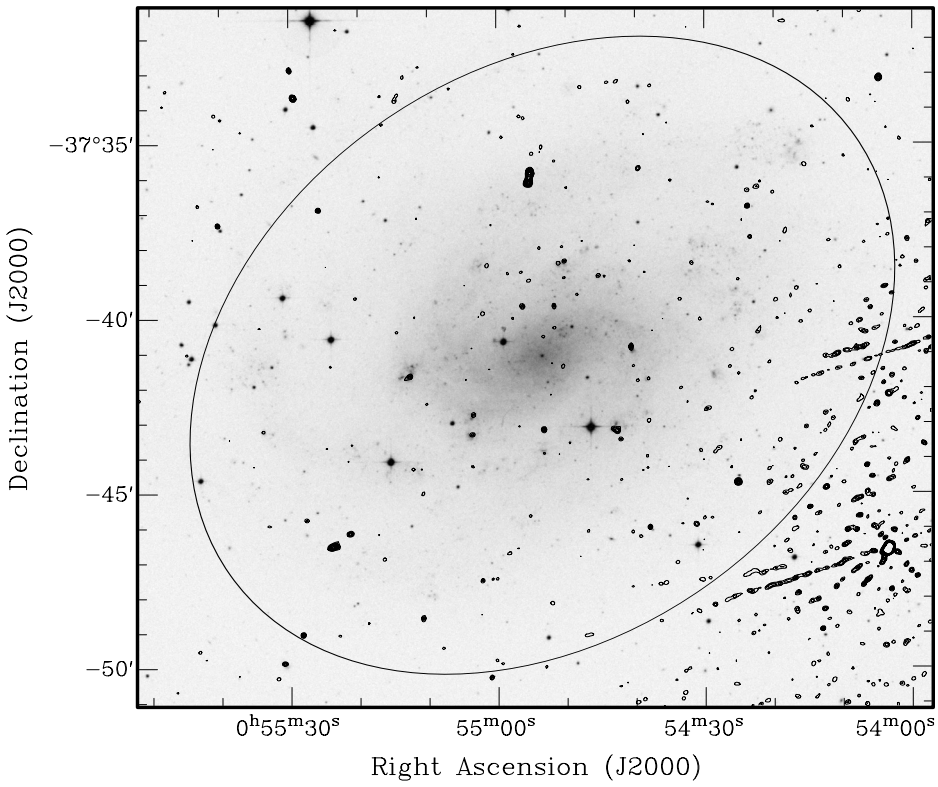

Fig. 1. ATCA 1374 MHz contours overlaying an DSS2-Red (R) image (grey scale) of NGC 300. An ellipse ($21.9' \times 15.5'$) overlay centered on the galaxy at RA(J2000) = $00^h54^m53.48^s$ Dec(J2000) = $-37°41'3.8''$ provides a visual boundary. Flux from two nearby contaminating sources, NVSS J005403–374636 and NVSS J005353–374020, can be seen in the bottom right-hand corner of the image. Contours are: 0.2, 0.3, 0.4, 0.5, 0.7, 1, 1.5, 2, 3, 4 and 5 mJy beam^{-1}. This image has a 1σ noise value of 0.058 mJy beam^{-1}.

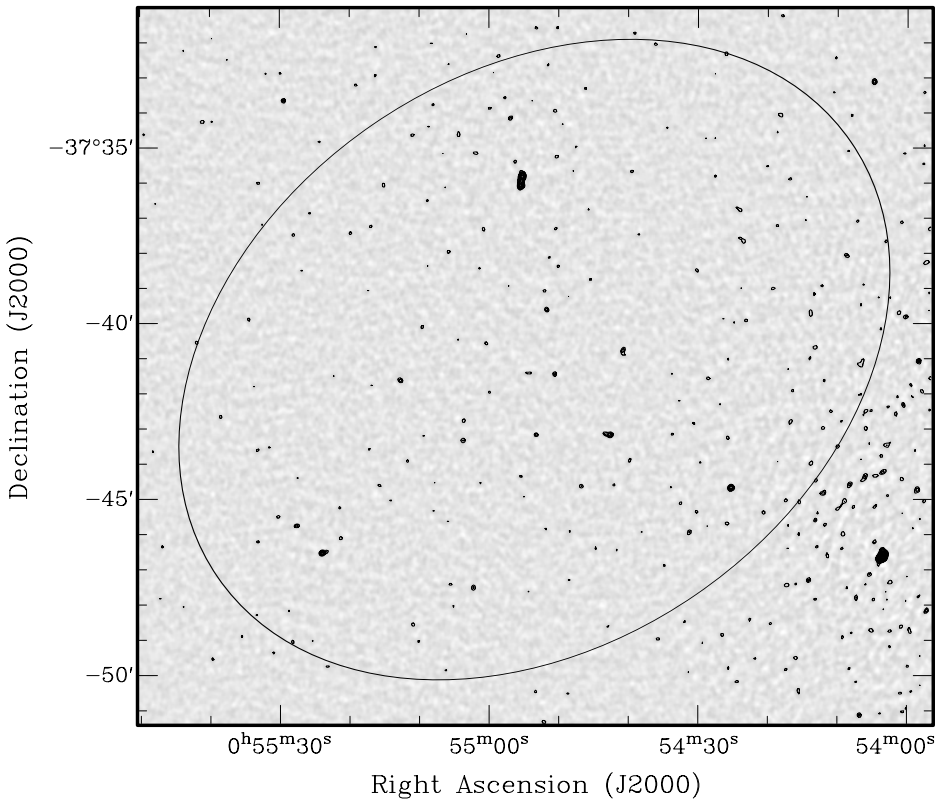

Fig. 2. The ATCA 2496 MHz image of NGC 300 bounded by our ellipse with its contours. Flux from two nearby contaminating sources, NVSS J005403–374636 and NVSS J005353–374020, can be seen in the bottom right-hand corner of the image. Contours are: 0.2, 0.3, 0.4, 0.5, 0.7, 1, 1.5, 2, 3, 4 and 5 mJy beam^{-1}. This image has a 1σ noise value of 0.062 mJy beam^{-1}.

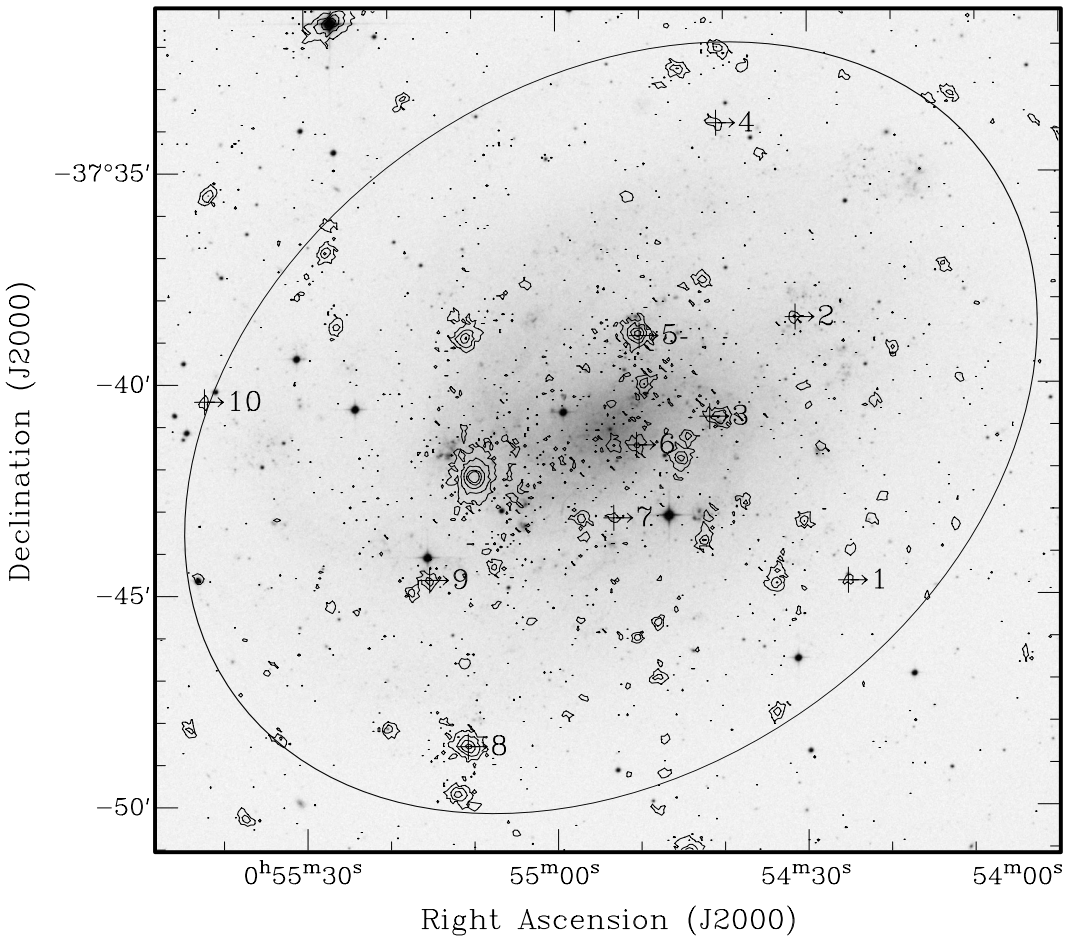

Fig. 3. *XMM-Newton* (energy range 0.3–6.0 keV) image (contours) of NGC 300 bounded by our ellipse overlaid on DSS2-Red (*R*) image (gray scale). Radio identifications are marked and X-ray contours are: 1.9, 5.8, 17.3, 52.2 and 104.3 in units of 10^{-2} cnts s^{-1} $arcmin^{-2}$. The resolution of the X-ray image is 4″.

time interval" (gti) files by removing times associated with contamination from flaring particles.

Source detection (SAS's edetect chain) was accomplished using the combined (both observations) filtered event lists from MOS 1, MOS 2 and PN separately. During source detection, lists were generated using a minimum likelihood threshold of 15 (which corresponds to a Gaussian significance of ∼5.1σ). These were then combined to produce a source list. This allowed determination of the coordinates of preliminary X-ray sources. We found a total of 533 X-ray sources but further analysis is in preparation by one of us (S. Carpano). Ten (10) coinciding sources were chosen visually by comparing overlapping contours from the *XMM-Newton* and all four radio images using the KARMA software package.

For each of the *XMM-Newton* point-like sources that coincided with radio sources, count rates were determined from each individual detector by first extracting its filtered spectrum and background. Backscale calibration was automatically applied to these files. Response and auxiliary matrix files were created to calibrate the data to the instrumental response of the telescope. It is noted that occasional sources fell very near to the detectors grid; this may have affected a source's hardness ratio somewhat, but not as greatly as the count rate itself.

The total counts and net count rates for each source were found with the High Energy Astrophysics Science Archive Research Center's (HEAsoft's) XSPEC package in the full (0.3–6.0 keV), soft (0.3–1.0 keV), medium (1.0–2.0 keV) and hard (2.0–6.0 keV) energy bands.

2.2.2. ROSAT

The *ROSAT* archive contains several pointed PSPC and HRI observations centered close to the field of NGC 300. More details on the *ROSAT* mission can be found in Trümper (1983). The two nearest *ROSAT* PSPC (energy range 0.1–2.4 keV) observations which have the best angular resolution were used in this study. For more details of the PSPC observations see Table 3.

In Fig. 4 we show the *ROSAT* PSPC image ("hard" energy range 0.52–2.01 keV) of the NGC 300 region. It was obtained from combining the two PSPC observations and binned to 5″ pixels. Several *ROSAT* HRI observations were performed within the field of NGC 300 but lower exposure times (total of ∼40 ks) did not allow a deeper quantitative study than was obtained from the PSPC observations (total of ∼46 ks). For more

Table 3. Summary of X-ray observations of the region of NGC 300.

X-ray obs. date	Instrument	RA (J2000) h m s	Dec (J2000) ° ′ ″	Exp (s)
28-11-1991	PSPC	00 54 52	–37 41 24	9324
26-05-1992	PSPC	00 54 52	–37 41 24	36 693
08-06-1994	HRI	00 54 52	–37 41 24	15 224
27-05-1995	HRI	00 54 52	–37 41 24	19 138
02-06-1997	HRI	00 54 52	–37 41 24	5619
27-12-2000	XMM–rev 192	00 54 56	–37 41 09	36 909
02-01-2001	XMM–rev 195	00 54 56	–37 41 10	46 711

details on the PSPC and HRI observations, see Read & Pietsch (2001).

3. Source analysis

We conducted the multi-frequency analysis of ATCA (1374 and 2496 MHz) and VLA (1448 and 4860 MHz) sources by identifying source positions with data from previous catalogues and our *XMM-Newton* data. These catalogues include optical observations by BL97, Soffner et al. (1996), Kim et al. (2002), Pietrzyński et al. (2001) and Deharveng et al. (1988); radio analysis by PDL and X-ray data from Read & Pietsch (2001).

Initially, we assume all radio images have a positional accuracy of less than 1″. Then, utilizing the viewer in the Karma software package (Gooch 1996), sources were selected using multi-frequency contour levels and catalogue annotation files overlaying a DSS2-Red (R)[1] image of the galaxy. A elliptical visual boundary to NGC 300 of 21.9′ × 15.5′, centered on RA(J2000) = $00^h54^m53.48^s$ Dec(J2000) = −37°41′03.8″, is provided by the NASA/IPAC Extragalactic Database (Jet Propulsion Laboratory, California Institute of Technology and National Aeronautics and Space Administration). A grid annotation file allowed systematic visualisation of each source field such that no region would be missed.

3.1. Radio sources

After converting VLA images to MIRIAD format, task IMSTAT was used to determine the rms sensitivity of all datasets individually by averaging several large quiet regions. We found sensitivity values of 0.058, 0.062, 0.066 and 0.037 mJy beam^{-1} for frequencies of 1374, 2496, 1465 and 4885 MHz, respectively. Assuming a distance of 2.02 Mpc (Freedman et al. 2001), this corresponds to luminosity limits of 2.83×10^{16}, 3.03×10^{16}, 3.22×10^{16} and 1.81×10^{16} W Hz^{-1}. In our visual selection of radio sources in this galaxy, we were also required to account for poorly cleaned sidelobes from two nearby radio sources, NVSS J005403-374636 and NVSS J005353-374020.

The position and flux density for each source at a given radio frequency were determined using the two-dimensional point-fitting algorithms in the MIRIAD software package with primary beam corrected images. This involved creating a region using task CGCURS, containing only the selected source, and analyzing this region with task IMFIT to find the source's flux density (with errors) and position. Since 20% of our sources are extended beyond image resolution, a Gaussian fitting process must include integration over the entire area of the object.

Estimates of the spectral index (α) of each radio feature/source were made based on flux densities obtained from corresponding radio-frequencies. (The spectral index α is defined by the relation $S_\nu \propto \nu^\alpha$, where S_ν is the integrated flux density and ν is frequency.) This process was accomplished using a standard line of best fit algorithm. Errors ($\Delta\alpha$) were deduced given the scatter in flux density and errors in individual flux density estimates.

We list in Table 4, for each of 54 detected radio objects; source number, position (RA and Dec), integrated flux densities (1374, 1448, 2496 and 4860 MHz) and corresponding errors, spectral index and error, source type, comparisons to BL97 images and identifications with sources at other wavelengths.

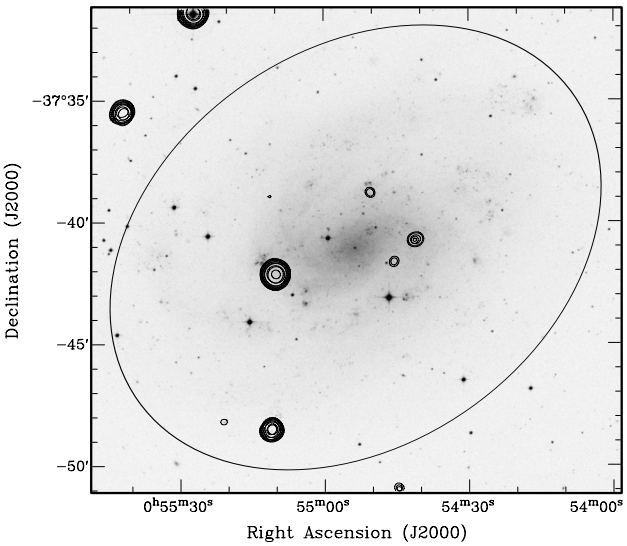

Fig. 4. *ROSAT* PSPC (energy range 0.52–2.01 keV, 46 ks) image (contours) of NGC 300 bounded by our ellipse overlaid on DSS2-Red (R) image (gray scale). Contours are: 1.4, 1.6, 2.0, 2.7, 3.8, 6.9, 12.8, 24.9, 48.9, 97.0 and 193.2 in units of 10^{-3} cnts s^{-1} arcmin^{-2}. The resolution of the X-ray image is 5″.

3.2. X-ray sources

Using the methods described above we found ten *XMM-Newton* X-ray sources in the area of NGC 300 having radio-continuum counterparts within an estimated *XMM-Newton* positional error of ∼4″. We present a contour image of *XMM-Newton* observations of NGC 300 in Fig. 3 and Table 6 lists the X-ray sources that match our radio sources.

For point like sources with more than 200 counts per observation, we were able to fit simple spectral models to the combined data for each observation using XSPEC after grouping the data to a minimum of 25 counts. Using this technique it was possible to fit a spectrum to two X-ray sources,

[1] This all sky survey is composed of digitized 15 μm scans from Schmidt Plates which cover almost the entire sky. More information about this survey and its data can be found at
http://arch-http.hq.eso.org/dss/eso-dss.html

Table 4. Measured radio-continuum properties of objects within NGC 300. Listed positions (RA and Dec) are from 1374 MHz observations where possible. In Col. 10, visual comparisons are made to BL97 [S II] versus Hα (with some contamination from [N II]) images; 0 = No flux, VF = very faint flux, F = faint flux, M = medium flux and S = strong flux. Prefixes to source numbers used in Col. 11: H = HRI (Read & Pietsch 2001), P = PSPC (Read & Pietsch 2001), D = Deharveng et al. (1988), S = Soffner et al. (1996), DSS2-Red(f/m) = STScI Digitized Sky Survey (1993, 1994), BL = Blair & Long (1997), RPS97 = Read et al. (1997), PSNR = Pannuti et al. (2000), GC = Kim et al. (2002), AS_ = Pietrzyński et al. (2001) and XMM = this Paper. Source type abbreviations are: SNR = supernova remnant, HII = H II region, BKG = background object and xrb = X-ray binary (capital letters denote higher confidence). †– denotes snr candidates.

1 ATCA source number	2 RA (J2000) h m s	3 Dec (J2000) ° ′ ″	4 $S_{1374\,\mathrm{MHz}}$ (mJy)	5 $S_{1448\,\mathrm{MHz}}$ (mJy)	6 $S_{2496\,\mathrm{MHz}}$ (mJy)	7 $S_{4860\,\mathrm{MHz}}$ (mJy)	8 $\alpha \pm \Delta\alpha$	9 Source Type	10 [S II]/Hα (BL)	11 Identifications
J005408.6–373804	00 54 08.69	–37 38 04.7			0.61 ± 0.01					DSS2-Red(f)
J005422.5–373615	00 54 22.53	–37 36 15.1	1.37 ± 0.04						0/VF	
J005423.4–373741	00 54 23.48	–37 37 41.4	0.41 ± 0.02	0.38 ± 0.06	0.40 ± 0.06		+0.0 ± 0.1	hii/bkg	0/0	
J005423.8–373648	00 54 23.84	–37 36 48.4	0.64 ± 0.02	0.58 ± 0.06	0.40 ± 0.04		–0.7 ± 0.1	snr†	0/0	
J005423.8–373621	00 54 23.88	–37 36 21.1	0.33 ± 0.01						0/0	
J005425.2–374441	00 54 25.25	–37 44 41.9	2.44 ± 0.10	2.55 ± 0.10	2.02 ± 0.09	0.23 ± 0.03	–1.8 ± 0.5	BKG		XMM1
J005431.2–374554	00 54 31.28	–37 45 54.6	0.41 ± 0.03	0.33 ± 0.04	0.44 ± 0.03		+0.3 ± 0.4	hii/bkg		
J005431.9–373825	00 54 31.91	–37 38 25.9	0.30 ± 0.02					SNR	F/F	P29(HR2 = 0.15), BL-S6([S II]/Hα = 0.60), XMM2, AS_18
J005437.9–374559	00 54 37.99	–37 45 59.5	0.65 ± 0.03	0.66 ± 0.06	0.27 ± 0.02		–1.5 ± 0.2	bkg	0/0	
J005438.1–374144	00 54 38.16	–37 41 44.2	0.27 ± 0.02	0.34 ± 0.06		0.11 ± 0.01	–0.8 ± 0.2	SNR/HII	F/S	S(west)31, D39, DSS2-Red(f), PSNR2(R1), AS_25
J005438.4–374240	00 54 38.49	–37 42 40.5		0.33 ± 0.02				snr/HII	F/F	D40, PSNR3(R2), RPS97(No. 2), AS_26a
J005439.6–373543	00 54 39.61	–37 35 43.4	0.42 ± 0.02	0.43 ± 0.10	0.33 ± 0.02		–0.4 ± 0.1	snr†	0/0	
J005440.6–374049	00 54 40.68	–37 40 49.7	0.56 ± 0.03	0.30 ± 0.05	0.38 ± 0.06	0.21 ± 0.01	–0.5 ± 0.3	SNR/HII	M/M	P38(HR2 = –0.33), BL-S10([S II]/Hα = 0.67), XMM3, H11, S(west)22, DSS2-Red(f), AS_29
J005441.0–373348	00 54 41.05	–37 33 48.9	0.29 ± 0.02	0.33 ± 0.05				bkg/snr	0/0	XMM4
J005442.7–374313	00 54 42.70	–37 43 13.3	0.63 ± 0.07	0.69 ± 0.06	0.65 ± 0.04	0.21 ± 0.02	–0.9 ± 0.3	SNR/HII	M/S	D53B, DSS2-Red(m), BL-S11([S II]/Hα = 0.53), AS_34
J005443.1–374311	00 54 43.11	–37 43 11.0	0.59 ± 0.08	0.75 ± 0.05	0.43 ± 0.03	0.32 ± 0.03	–0.6 ± 0.2	SNR/HII	M/S	D53A, PSNR4(R3), DSS2-Red(s), AS_34
J005445.3–373842	00 54 45.31	–37 38 42.8				0.17 ± 0.03		HII	0/0	D62, AS_45
J005445.3–373847	00 54 45.39	–37 38 47.1	0.30 ± 0.03		0.25 ± 0.01		–0.3 ± 0.1	SNR/HII	F/S	D61, DSS2-Red(m), AS_45
J005448.0–373323	00 54 48.01	–37 33 23.7	0.31 ± 0.03	0.37 ± 0.07					0/0	DSS2-Red(f)
J005450.2–374030	00 54 50.28	–37 40 30.0		0.73 ± 0.09		0.39 ± 0.01	–0.5 ± 0.2	SNR/HII	M/S	D76A, PSNR7(R6), DSS2-Red(m), AS_56
J005450.3–373822	00 54 50.30	–37 38 22.4	0.36 ± 0.05	0.23 ± 0.01	0.25 ± 0.01	0.23 ± 0.03	–0.2 ± 0.2	SNR/HII	M/S	D77, DSS2-Red(m), AS_52a
J005450.3–373850	00 54 50.35	–37 38 50.9	0.24 ± 0.02					xrb	M/F	DSS2-Red(f)P32(HR2 = 0.75), H10, XMM5, AS_52
J005450.5–374123	00 54 50.52	–37 41 23.0	0.28 ± 0.02	0.30 ± 0.03	0.37 ± 0.02		+0.4 ± 0.1	hii/bkg	0/0	XMM6
J005450.7–374022	00 54 50.73	–37 40 22.2	0.19 ± 0.01			0.13 ± 0.01	–0.3 ± 0.1	SNR/HII	F/F	DSS2-Red(f), D76B, AS_56b
J005450.8–374015	00 54 50.82	–37 40 15.1				0.14 ± 0.02		HII	VF/VF	D76B, AS_56b
J005451.1–373826	00 54 51.16	–37 38 26.1	0.95 ± 0.05	0.33 ± 0.01		0.14 ± 0.02	–1.2 ± 0.7	SNR/HII	M/S	D79, DSS2-Red(m), AS_52d
J005451.3–374621	00 54 51.34	–37 46 21.9		0.24 ± 0.02				HII	VF/S	PSNR10(R9), D82, DSS2-Red(f)
J005451.7–373939	00 54 51.79	–37 39 39.6	0.35 ± 0.03	0.46 ± 0.03	0.40 ± 0.02	0.33 ± 0.04	–0.1 ± 0.2	SNR/HII	M/S	DSS2-Red(s), D84, PSNR11(R10), GC6, AS_57
J005453.3–374311	00 54 53.30	–37 43 11.9	0.69 ± 0.04	0.66 ± 0.06	0.43 ± 0.03	0.12 ± 0.01	–1.4 ± 0.2	BKG	M/F	DSS2-Red(m), XMM7, GC7
J005455.3–373557	00 54 55.32	–37 35 57.5	17.88 ± 1.31	16.78 ± 1.06	10.18 ± 0.83	2.01 ± 0.13	–1.7 ± 0.3	bkg	0/0	
J005456.3–373940	00 54 56.36	–37 39 40.0	0.39 ± 0.04	0.68 ± 0.06				HII	M/F	DSS2-Red(m), D99
J005456.7–373413	00 54 56.77	–37 34 13.8	0.28 ± 0.03	0.31 ± 0.06	0.49 ± 0.04		+0.9 ± 0.1	hii/bkg	0/0	
J005500.5–374037	00 55 00.58	–37 40 37.4	0.20 ± 0.01		0.25 ± 0.01	0.12 ± 0.01	–0.4 ± 0.4	SNR/HII	F/S	DSS2-Red(m), D109, S(east)20, AS_76
J005500.7–374143	00 55 00.73	–37 41 43.5	0.20 ± 0.01					HII	VF/S	DSS2-Red(f), S(east)19, D111
J005500.9–373720	00 55 00.93	–37 37 20.1	0.22 ± 0.01	0.29 ± 0.04	0.30 ± 0.01		+0.3 ± 0.4	hii/bkg	0/0	
J005501.4–373829	00 55 01.49	–37 38 29.9	0.84 ± 0.02		0.48 ± 0.06		–0.9 ± 0.1	SNR	0/0	AS_82
J005502.1–373952	00 55 02.13	–37 39 52.4	0.89 ± 0.04						0/0	
J005502.2–374731	00 55 02.25	–37 47 31.0	0.36 ± 0.03	0.26 ± 0.02	0.44 ± 0.02		+0.6 ± 0.5	hii/bkg	0/0	
J005503.5–374246	00 55 03.50	–37 42 46.0	0.34 ± 0.02	0.41 ± 0.03	0.31 ± 0.01	0.24 ± 0.03	–0.4 ± 0.1	SNR/HII	F/S	DSS2-Red(m), D118A,PSNR12(R11), AS_84
J005503.6–374320	00 55 03.66	–37 43 20.1	0.33 ± 0.03	0.32 ± 0.04	0.34 ± 0.02	0.13 ± 0.02	–0.7 ± 0.3	SNR/HII	M/S	D119A, DSS2-Red(m), PSNR13(R12), AS_86
J005507.3–374106	00 55 07.30	–37 41 06.1				0.14 ± 0.01		HII	VF/M	DSS2-Red(f), D126, S(east)4, AS_94
J005510.8–374835	00 55 10.85	–37 48 35.3	0.52 ± 0.04	0.30 ± 0.05	0.45 ± 0.01		+0.2 ± 0.9	AGN		DSS2-Red(f), P58(HR2 = 0.01), H16, XMM8
J005512.3–373908	00 55 12.37	–37 39 08.5			0.26 ± 0.01			HII	0/F	DSS2-Red(f), D136
J005512.7–374140	00 55 12.70	–37 41 40.3	0.49 ± 0.04	0.55 ± 0.01	0.41 ± 0.03	0.21 ± 0.02	–0.7 ± 0.1	SNR/HII	M/S	DSS2-Red(m), PSNR14(R13), D137A, AS_102b
J005515.4–374439	00 55 15.40	–37 44 39.2	0.20 ± 0.01	0.22 ± 0.02				SNR/HII	S/S	D141,P49(HR2 = –0.16), XMM9, BL-S26([S II]/Hα = 0.57), DSS2-Red(f), AS_107
J005516.4–374653	00 55 16.45	–37 46 53.7	0.34 ± 0.02						VF/VF	
J005521.3–374609	00 55 21.35	–37 46 09.6	0.67 ± 0.03	0.76 ± 0.11	0.41 ± 0.02		–1.0 ± 0.3	bkg/snr	0/0	
J005523.9–374632	00 55 23.95	–37 46 32.4	2.23 ± 0.17	2.10 ± 0.29	1.33 ± 0.22		–0.9 ± 0.1	bkg/snr	0/0	
J005525.8-373653	00 55 25.82	–37 36 53.8	0.63 ± 0.05	0.55 ± 0.05	0.33 ± 0.02		–1.0 ± 0.1	bkg/snr		
J005527.6–374546	00 55 27.66	–37 45 46.4	0.36 ± 0.03	0.30 ± 0.01	0.60 ± 0.02		+1.0 ± 0.4	hii/bkg		
J005528.2–374903	00 55 28.25	–37 49 03.3	0.96 ± 0.05	0.77 ± 0.06	0.61 ± 0.03		–0.6 ± 0.3	snr†		
J005533.6–374147	00 55 33.65	–37 41 47.8			0.39 ± 0.02			HII	0/F	D158, DSS2-Red(f)
J005533.8–374314	00 55 33.87	–37 43 14.6	0.27 ± 0.01					SNR/HII	M/S	D159, BL-S28([S II]/Hα = 0.61), DSS2-Red(f), AS_113
J005541.9–374033	00 55 41.94	–37 40 33.5			1.24 ± 0.04			snr	0/0	P36(HR2 = –0.26), XMM10

Table 5. *XMM-Newton* photoelectric absorption model fits to radio counterparts in NGC 300 (1σ confidence interval using MOS 1, MOS 2 and PN data). Source XMM5 was also found to closely fit a power law spectrum. The corresponding values for this model are shown in parentheses.

Spectral fits					
		Bremsstrahlung		Power law	
Source number	Revolution number	Column (10^{20} cm^{-2})	Temperature (keV)	Column (10^{20} cm^{-2})	Index
XMM5	192	$22.6^{+4.1}_{-3.1}$	$5.0^{+1.2}_{-0.9}$	(30.4)	(1.9)
XMM8	192			$9.1^{+4.5}_{-3.1}$	$2.8^{+0.4}_{-0.2}$
XMM5	195	$28.1^{+4.1}_{-3.2}$	$5.2^{+1.0}_{-1.0}$	(37.4)	(1.9)
XMM8	195			$10.3^{+2.5}_{-2.0}$	$2.8^{+0.1}_{-0.1}$

XMMU J005450.0–373853 and XMMU J005510.7–374835 (our XMM5 and XMM8, respectively). As Table 5 shows, we find the best spectral fit for XMM5 to be the photoelectric absorption with bremsstrahlung model although the photoelectric absorption with power law model was a nearly as good. For XMM8, the best fit was clearly the photoelectric absorption with power law model.

Spectral fitting was more difficult for sources having few counts (<200). For these sources, we used hardness ratios to give some indication of their X-ray spectra. Using our energy bands: soft (0.3–1.0 keV), medium (1.0–2.0 keV) and hard (2.0–6.0 keV); HR1 was defined as the ratio of the difference of medium and soft counts to their sum ((med–soft)/(med+soft)). In similar fashion, HR2 was defined as the ratio of the differences of hard and soft counts to their sum ((hard–soft)/(hard+soft)). Table 6 shows the results of these calculations for data obtained from the PN detector for each observation.

Figure 5 shows a colour–colour diagram of HR1 vs. HR2 for each source and observation. Numerous authors including Haberl et al. (2000) have created similar diagrams to establish a relation between various types of sources including supersoft sources, foreground stars, X-ray binaries and SNRs, utilizing *ROSAT* observations of the Magellanic Clouds. The definitions of HR1 and HR2 vary with different X-ray telescopes and so it is not possible to use *ROSAT* source type criteria with *XMM-Newton* data.

Kong & Di Stefano (2003, and reference therein) have created *XMM-Newton* colour–colour diagrams in their analysis of IC 342 with energy bands and hardness ratios similar to ours. Superimposed models in their Fig. 4 colour–colour diagram shows that power law spectra tend to occupy the top right section while soft thermal models occupy the lower left. For each of their models, the column density increases from left to right. We used XSPEC's "fakeit" command to create our own simulated simple model spectra for our colour–colour diagram shown in Fig. 5.

Our hardness ratios primarily add insight to previously selected SNRs as the colours of the X-ray sources are not reliable enough to identify source type alone. It must be remembered that this exercise tells us only about the spectrum of these objects. Recent observations of Galactic SNRs such as RX J1713.7–3946 and SN 1006 (Koyama et al. 1997) have shown that they can have non-thermal as well as thermal properties in X-ray.

3.3. Identifications

Table 7 lists the number of sources in common with our data and other (optical and X-ray) catalogues. This information was compiled from both visual inspection of our data and annotation files (created from the literature) using KARMA's kview.

Positional identifications with published sources in the optical and X-ray domains were considered high if they fell within the positional limits of these surveys (~4″). An exception was the *ROSAT* catalogue created by Read & Pietsch (2001) who cite positional errors for each of their X-ray sources individually. Annotation circles were created for this catalogue with a radius corresponding to these errors in order to find each corresponding radio source. Next, each individual source identification was carefully reexamined using contour levels from different wavelengths before being added to our list.

Using this process, an interesting systematic error is suspected with respect to data presented by Soffner et al. (1996) and Deharveng et al. (1988). When a correction of δDec = –3.9″ was applied to each of these datasets, the respective positions of their sources matched the DSS2-Red (*R*) plate almost exactly. It seems reasonable that errors of this magnitude occur in the literature presumably due to registration of their optical image on the sky astrometric frame.

As a matter of background, we now discuss catalogues of NGC 300 found in the literature in more detail. BL97 detected 28 SNRs candidates through CCD imagery with interference filters to isolate emission from Hα + [N II], [S II] and a continuum near 610 nm, to identify isolated nebulae bright in [S II] relative to Hα. Optical long-slit CCD spectra of these candidates confirmed that these sources met the usual criteria of a flux ratio ([S II]/Hα) of 0.4 or greater. (All five BL97 SNRs which match our radio sources have ratios exceeding 0.57.) As noted in Gordon et al. (1999), the physical basis for this is that in photoionized regions, most sulfur is in the doubly ionized state. By contrast, in shock-heated nebulae, the cooling time is short so that many ionization states occur, including S^+. This causes us to observe higher [S II]/Hα ratios in SNRs than in H II regions. In this study we use BL97 1500s images transferred from tape to help characterize our sources.

BL97 also determined the optical diameter for their sources, noting that the majority of the objects were reasonably well resolved. They based their measurements on the earlier distance value of 2.1 Mpc, noting that the smallest SNRs in NGC 300 are at the seeing disk value of 1.5″ (1″ = 10.2 pc). These apparent diameters should be considered upper limits. The majority of BL97 SNRs have apparent diameters in the 25–75 pc range, which they felt reflected a well-evolved ISM-dominated population for which their search technique worked best. However, BL97 reported four (4) large SNRs in NGC 300 with diameters in the 75–200 pc range for which there are no Galactic counterparts; a trend also seen in other galaxies (e.g. M 33). These objects may represent

Table 6. *XMM-Newton* sources found to match our radio sources showing PN detector hardness ratios and count rates. A complete catalogue of *XMM-Newton* sources can be found in Carpano (in preparation). Column 4 abbreviation Pe represents the estimated positional error.

(1)	(2)	(3)	(4)	(5)			(6)		
Source number	RA (J2000)	Dec (J2000)	Pe	Revolution 192			Revolution 195		
(XMMU)	h m s	° ′ ″	(″)	Tot (cnt/ks)	HR1	HR2	Tot (cnt/ks)	HR1	HR2
XMM1 / J005425.2–374441	00 54 25.20	–37 44 41.1	0.9	1.13	–0.26	–1.00	1.47	–0.13	–0.25
XMM2 / J005431.4–373827	00 54 31.45	–37 38 27.0	0.7	0.62	–0.01	–0.60	1.76	+0.04	–0.19
XMM3 / J005441.6–374048	00 54 41.69	–37 40 48.0	1.5	1.27	–0.63	–0.99	1.63	–0.58	–1.00
XMM4 / J005440.8–373351	00 54 40.85	–37 33 51.3	0.8	1.39	+0.84	+0.94	0.72	+0.31	+0.62
XMM5 / J005450.0–373853	00 54 50.08	–37 38 53.2	0.1	28.39	+0.31	+0.11	20.62	+0.35	+0.19
XMM6 / J005450.4–374128	00 54 50.45	–37 41 28.4	0.6	2.02	–0.48	–0.92	2.23	–0.64	–1.00
XMM7 / J005453.2–374311	00 54 53.21	–37 43 11.8	0.8	0.88	–0.34	+0.79	1.27	–0.35	+0.02
XMM8 / J005510.7–374835	00 55 10.75	–37 48 35.8	0.3	27.16	–0.37	–0.75	29.83	–0.43	–0.73
XMM9 / J005515.2–374439	00 55 15.27	–37 44 39.6	0.4	5.36	–0.69	–0.95	0.93	–1.00	–0.98
XMM10 / J005542.0–374025	00 55 42.04	–37 40 25.6	0.7	2.35	–0.76	–0.88	1.08	–0.88	–0.93

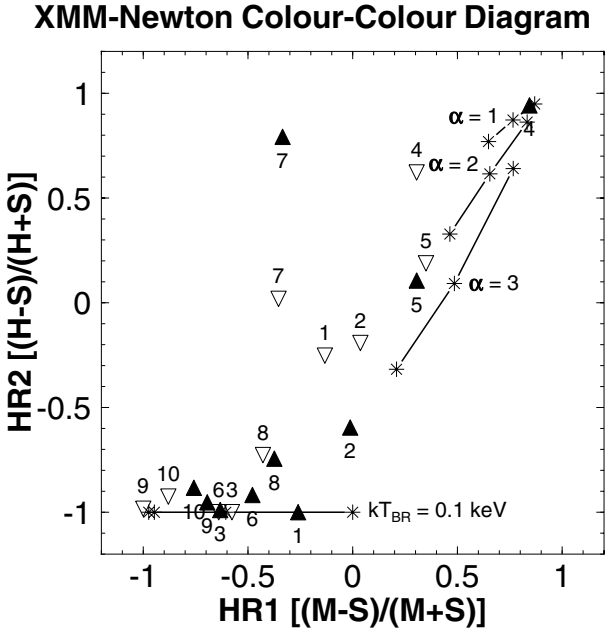

Fig. 5. Colour–colour diagram for all correlated *XMM-Newton* sources using PN hardness ratios. Each source is numbered while filled triangles indicate sources from revolution 192 and open triangles represent those from revolution 195. The estimated hardness ratios from different models are shown as lines connected to "fake" data points (stars). Power law models tend to have hardness ratios in the upper right of the diagram while thermal models have ratios in the lower left of the diagram.

superbubbles; remnants formed from more than one supernova explosion along with stellar winds found in a group of massive stars. Dunne et al. (2001) have studied X-rays from superbubbles of about the same size located within the Large Magellanic Clouds and found that the X-ray emission is brighter than that theoretically expected for a wind-blown bubble alone, suggesting that the X-ray emission has been enhanced by interactions with several SNRs of similar age.

Hα images were used to determine H II regions in NGC 300 by Deharveng et al. (1988) and Soffner et al. (1996). Deharveng et al. (1988) cataloged 176 H II regions within NGC 300 while Soffner et al. (1996) report finding 90. In addition, Soffner et al. (1996) show 31 counterpart regions reported in Deharveng et al. (1988).

Related to these H II regions, OB associations composed of groups of young, massive, gravitationally unbound stars formed from molecular clouds within NGC 300 were studied by Pietrzyński et al. (2001). Using the Path Linkage Criterion (PLC), they found 117 such associations. These OB associations were reported to overlap with at least 60% of the H II regions found by Deharveng et al. (1988). Pietrzyński et al. (2001) note that these associations are well suited as tracers of recent or ongoing star formation. In our analysis, we find (Table 4) 22 OB associations that correspond to either H II regions or SNRs.

We are mindful to distinguish these H II regions and OB associations from other objects near NGC 300. Kim et al. (2002) found 17 globular cluster candidates in NGC 300 using *U BV I* CCD photometry. Their search used photometric information, morphological parameters and visual inspection, and they note that the globular clusters were barely resolved in their images.

Results from *ROSAT* PSPC and HRI X-ray observations of NGC 300 have been presented by Read & Pietsch (2001). A summary of X-ray sources and their properties from the *ROSAT* PSPC image (Fig. 4) is presented in their Table 2.

3.4. Multi-wavelength selection criteria

Multi-frequency analysis enhances our understanding of the nature of discrete sources in NGC 300. We assume that this galaxy is essentially transparent to radio emission, and, radio and X-ray catalogues contain not only sources located within NGC 300, but also background sources lying behind it. We use a similar classification to that used by Filipović et al. (1998) to divide the radio sources into two major groups:

1. non-thermal sources, such as:
   a) background quasars and galaxies
   b) SNRs within NGC 300;
2. thermal sources, such as H II regions within NGC 300.

With this in mind, we used the spectral index obtained from our ATCA and VLA radio data to aid in the classification of each

Table 7. Results of multi-frequency source comparison. Numbers represent sources in common to two surveys. *XMM-Newton* sources are in "()" if not confirmed. Abbreviations used are: *ROSAT* = Read & Pietsch (2001); D = Deharveng et al. (1988); S = Soffner et al. (1996), DSS2-Red(f/m) = STScI Digitized Sky Survey (1993, 1994), BL = Blair & Long (1997), *XMM-Newton* = this paper, K = Kim et al. (2002) and P = Pietrzyński et al. (2001).

	ATCA 20 cm	VLA 20 cm	ATCA 13 cm	VLA 6 cm	*XMM-Newton*	*ROSAT*-PSPC	*ROSAT*-HRI	BL	D	S	K	P	DSS2-Red(f/m)
ATCA 20 cm	44	32	29	15	9	5	3	5	16	4	2	18	21
VLA 20 cm	32	35	26	14	7	3	2	3	14	2	2	13	17
ATCA 13 cm	29	26	33	12	6	3	2	2	11	2	2	11	15
VLA 6 cm	15	14	12	19	3	1	1	2	15	4	2	16	15
XMM-Newton	9	7	6	3	(533)	(25)	(7)	(6)	(4)	(6)	(1)	(11)	–

Table 8. Selection criteria for radio source type. Note use of logical AND and OR for this table.

Source type	Selection criteria	
SNR	a) $\alpha \leq -0.2$ AND H II / OB Association	OR
	b) Known Optical SNR	
snr	a) $-0.8 \leq \alpha \leq -0.2$ ("radio snr candidate")	OR
	b) X-ray Source	
HII	a) Known From Optical (Deharveng / Soffner)	
hii	a) $\alpha \geq -0.2$	
BKG	a) $\alpha \leq -0.8$ AND X-ray	OR
	b) Known From X-ray / Radio Study	
bkg	a) X-ray Source	OR
	b) $\alpha \geq -0.2$	OR
	c) $\alpha \leq -0.8$	

source into the above categories using the following criteria based on McGee & Newton (1972):

(i) Background sources with $\alpha \leq -0.8$;
(ii) SNRs with a steep spectrum $-0.8 \leq \alpha \leq -0.2$; and
(iii) H II regions with a flat spectrum, $\alpha \geq -0.2$, although background radio sources can also have a flat spectrum.

Sources cannot be classified by radio spectral index alone due to large overlaps between various source types and spectral index errors. H II regions and SNRs are often associated since the latter may be embedded in or near the former. Further, PDL requires that a radio source be associated with a region of Hα emission in order to differentiate background radio sources from those intrinsic to NGC 300.

Therefore, we use our *XMM-Newton* data, identifications from six other catalogues, DSS2-Red (*R*) images, original BL97 images and radio spectral index to create our classification. Because of the distance to NGC 300 (2.02 Mpc), we are unable to use source extension and morphology as part of our criteria.

Specifically, we used the following classification scheme (Table 8) to classify each source within the area of NGC 300 defined by our ellipse:

(i) **For background sources:** If a source with a very steep spectral index ($\alpha \leq -0.8$) was found to have an identification in the X-ray domain, it was designated as a background source or "BKG". If no spectral index could be calculated because the source was too faint at other radio wavelengths, then catalogue identifications were used to determine if the source *could* be a background object. If no resolution using this information was possible, these sources were not designated. Sources with a steep radio spectral index but no other identifications were designated as "bkg" as were those sources with a flat spectral index (due to the possible variability of background sources in general). We adopted the estimate given by PDL that approximately five background sources should have been observed in random directions through the disk of NGC 300 in the 20 cm image at a 3σ level of 0.2 mJy beam^{-1} or greater. (They based their estimate on work by Mitchell & Condon 1985, for the number density of background sources.)
(ii) **For H II regions:** Sources described in other catalogues as H II regions were designated as "HII". Sources with a flat radio spectral index that did not have identifications at other wavelengths or catalog descriptions were listed as "hii/bkg". The "hii" designation was required because DSS2-Red (*R*) or Hα images may not have been sensitive enough to show these potential H II regions. The "bkg" designation was included since these radio sources *could* be intrinsically variable with flat indices. Sources with a steeper (or borderline steeper) spectral index which were described as both H II regions (and possibly supernova remnants) in other catalogues were designated as "SNR/HII" since these most likely represent areas where a supernova remnant was embedded within or associated with an H II region. Most of these sources could be visually seen in BL97 [S II] images as discussed below although this alone did not classify the objects.
(iii) **For supernova remnants:** In addition to SNRs embedded within H II regions, a source known to be a supernova remnant from other catalogues was designated as "SNR" in Table 4. Our classification of a radio SNR candidate, "snr†" was based on spectral index when no identifications were found and did not include those sources that could have been a supernova remnant while just as likely another type of source, such as a background object. For example, ATCA J005525.8–373653 could be either a background source or SNR and was designated as "snr/bkg". This source was not included in our count of SNR candidates. Any source that had radio and X-ray

Table 9. Comparisons of positions including 95 percent confidence intervals (CI) and standard deviations. D = Deharveng et al. (1988).

Comparison	$\Delta\alpha$ ±CI (arcsec)	$\Delta\delta$ ± CI (arcsec)	SD α (arcsec)	SD δ (arcsec)	Notes
1374 MHz–1448 MHz	-0.0 ± 0.4	$+0.3 \pm 0.7$	1.1	2.0	32 matches
1374 MHz–2496 MHz	-0.0 ± 0.5	$+0.0 \pm 0.7$	1.4	1.8	30 matches
1374 MHz–4860 MHz	-0.0 ± 0.8	$+0.6 \pm 1.5$	1.4	2.6	15 matches
1374 MHz–H II	-0.7 ± 0.7	-0.5 ± 0.8	1.3	1.5	16 matches; D
1374 MHz–*XMM-Newton*	$+0.5 \pm 3.8$	-1.1 ± 1.6	4.9	2.1	9 matches

emission unexplained otherwise has "snr" (possible supernova remnant) as one of its designations.

4. Calibration procedures

4.1. Position calibration

The accuracy of the positions of all of our radio sources found by methods described in Sect. 3.1 is limited by the pointing accuracy and beam size of the ATCA and VLA telescopes. Since our criteria for radio source cross-identifications are based initially on a radius of less than 1″ and radio source cross-identifications with optical catalogues on less than 4″, we expect a small amount of scatter in position differences if there is true positional agreement.

We have compared the positions of 16 H II regions cited in Deharveng et al. (1988) (systematically corrected as discussed Sect. 3.1) to their ATCA counterparts at 1374 MHz and have found no significant positional bias between our radio positions and the published optical positions. At the 95 percent confidence level (using the student-t with $n - 1$ degrees of freedom), the positional differences in right ascension and declination ($\Delta\alpha$ and $\Delta\delta$, respectively) are $\Delta\alpha = -0.7'' \pm 0.7$, $\Delta\delta = -0.5'' \pm 0.8$. Comparisons of 1374 MHz positions with positions at the other radio frequencies and *XMM-Newton* show the radio catalogues to be self-consistent (Table 9).

4.2. Radio-continuum uncertainties in flux densities

In Fig. 6 we compare ATCA (1374 MHz) to VLA (1448 MHz) flux densities. We find the line of best fit for this data to be $S_{1448} = (-0.0155 \pm 0.017) + (0.979 \pm 0.04) S_{1374}$. There is no evidence for systematic differences in the flux densities from the ATCA and the VLA.

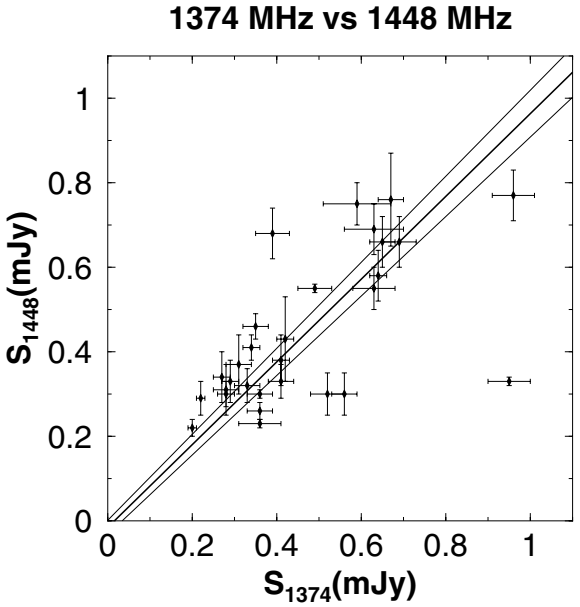

Fig. 6. Comparisons of flux density between ATCA (1374 MHz) and VLA (1448 MHz) sources with individual flux density error bars plotted on a linear scale. A weighted line of best fit is $(-0.0155 \pm 0.017) + (0.979 \pm 0.04)S_{1374}$. This graph shows all except the three strongest sources but all sources were used in statistical calculations.

5. Sources

5.1. Supernova remnants

5.1.1. Luminosity function of SNRs

Because of the relative certainty of the SNRs distance, the luminosity function is directly proportional to our observed flux densities. The luminosity of each radio source at a specific frequency, ν, is given in W Hz^{-1} and is defined by the relation:

$$L_\nu = 4\pi D^2 S_\nu \quad (1)$$

where D is the distance to NGC 300 of 2.02 Mpc (Freedman et al. 2001) and S_ν is the flux density at a given radio frequency. In our case, the source flux density at 1374 MHz was used to estimate the luminosity of each SNR source. The 5σ completeness level at this frequency is 0.29 mJy with a corresponding level in luminosity of 1.4×10^{17} W Hz^{-1}.

In Fig. 7 we show a histogram of 17 SNRs (ATCA J005450.2–374030 does not have a flux density at 1374 MHz). The mean luminosity of the SNRs is 2.05×10^{17} W Hz^{-1} with standard deviation 1.09×10^{17} W Hz^{-1}. Here, we are seeing only selected high luminosity sources just above the completeness level. Deeper studies are required for a complete sampling of SNRs in NGC 300.

5.1.2. Optically selected SNRs

Of the five BL97 SNRs identified with our sources, two (BL-S10, Fig. 8d and BL-S11, Fig. 8h) have radio spectral indices consistent with SNRs. We cannot determine a spectral index for the remaining three sources (BL-S6, Fig. 8a, BL-S26, Fig. 8v and BL-S28, Fig. 8u). Additionally, three of these BL97 sources (BL-S6, BL-S10 and BL-26) have corresponding X-ray emission. As noted by Chen & Chu (1998), only a small number of optically identified extragalactic SNRs can be confirmed at radio and X-ray wavelengths with these being among the most luminous remnants.

ATCA J005431.9–373825 corresponds to BL-S6 with a [S II]/Hα ratio of 0.60. This SNR coincides with an OB association and is seen both in *ROSAT* and *XMM-Newton* observations. Our colour–colour diagram is not helpful in determining the X-ray spectrum of this source and it contains too few counts for model fitting.

BL97's S10 identifies with ATCA J005440.6–374049 and is associated with an H II region and an OB association.

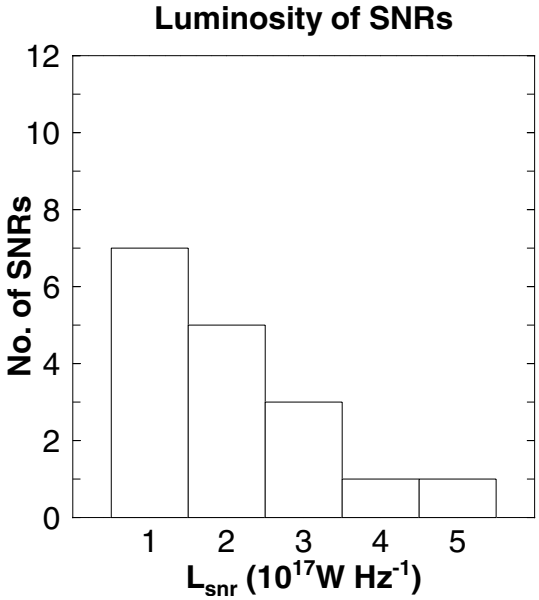

Fig. 7. Luminosity function of SNRs in NGC 300.

Read & Pietsch (2001) suggest that it is a soft source and our *XMM-Newton* data implies that it has a thermal spectrum. Our calculated radio spectral index of –0.5 is also consistent with an SNR.

ATCA J005515.4–374439 (BL-S26) also has a thermal spectrum by inspection of its *XMM-Newton* X-ray colour diagram (Fig. 5, XMM9) and is also labeled P49 in *ROSAT* observations (see Figs. 8v, 8w and 8x). Its radio spectral index cannot be reliably found since we only have flux densities for two very near frequencies (1374 and 1448 MHz).

In Table 7, we note a total of six (6) *XMM-Newton* sources with an existence likelihood of 15 which appear to be valid sources on visual inspection that match BL97 SNRs within a 4″ positional radius. Thus, possibly as many as three BL97 optical SNRs have X-ray emission but no radio detection. We also find four (4) and six (6) X-ray cross-matches within H II regions from Deharveng et al. (1988) and Soffner et al. (1996), respectively. Four BL97 SNRs with X-ray emission are associated with H II regions and only two of these have radio emission.

BL97 notes that while the canonical value of 0.4 in the ratio of [S II] to Hα has worked well in the Milky Way and Local Group galaxies to separate shock-heated nebulae from photoionized gas, the exact value of this cutoff has not been important since there is a gap in the distribution. Photoionized regions tend to show ratios of ∼0.2 or below. In Col. 10 of Table 4 we show the results of a visual inspection of original 1500 s plates from BL97. [S II] plates were also used to create optical backgrounds for our radio and X-ray contours shown in Fig. 8. Although not quantitative, we see [S II] emission from 12 sources other than the SNRs reported by them. H II regions without an SNR identification tend to show little or no [S II] emission.

Some of the more interesting objects in Fig. 8 not reported in BL97 include ATCA J005438.1-374144 (Fig. 8g), in which the typical spherical shape of a SNR can be seen. Radio emission (with a resolution of about 6″ compared to an optical resolution of 1.5″) with a spectral index of –0.8 is seen from the most intense area at "4 o'clock", highlighting that non-thermal radio emission from SNRs is formed at the shock. In fact, the expanding shell of a SNR may be undergoing different processes at the same time causing some areas to emit non-thermal radio radiation while other regions do not (also see the same process in BL-S28 shown in Fig. 8u). This may also be the case with sources ATCA J005450.2–374030 and ATCA J005450.7–374022. BL97 noted that there appeared to be 4 large SNRs in their data that measured up to 200 pc (20″). With these two sources, we may be detecting radio emission from one large SNR or superbubble (see Figs. 8k and 8l).

Radio emission from what appears to be a shell shock front is also seen in J005451.1–373826 (Fig. 8n) and J005500.5–374037 (Fig. 8p), with the latter having a more complete shell appearance. ATCA J005443.1–374311 (Fig. 8i), J005445.3–373847 (Fig. 8j), J005450.3–373822 (Fig. 8m), J005451.7–373939 (Fig. 8o), J005503.5–374246 (Fig. 8r) and J005512.7–374140 (Fig. 8t) have less defined shells. ATCA J005503.6–374320 (Fig. 8s) may show only a half shell in [S II], but this would put the diameter of the remnant at about 100 pc and its shape is not well defined.

We cannot determine [S II]: Hα ratios of the above sources from existing BL97 observations. We feel that optical long-slit CCD spectra from these SNRs initially found in our radio data and now suspected from visual inspection of BL97's [S II] images, would be helpful in their final determination as SNRs. This information might also fine tune the [S II]: Hα ratio cutoff between H II regions and SNRs.

5.1.3. Radio selected SNRs

We found thirteen additional SNRs than reported by BL97 based on radio spectral index and identification with H II regions or OB associations (Table 4). Although most of them have some optical emission as discussed above, there is a general lack of X-ray emission from this group of objects. This emphasizes that radio wavelengths are especially important for the detection these objects.

SNR ATCA J005451.7–373939 has a positional identification with both a globular cluster (GC6) and an OB association. It seems likely in this case, that the radio emission is associated with the OB association and the globular cluster is simply superimposed, since cluster SNRs most likely dissipated into the interstellar medium long ago.

5.2. Other interesting sources

We find three background sources based on positional identifications and spectral index. Although most of these sources represent distant galaxies, one of these, ATCA J005453.3–374311, is coincident with a globular cluster as reported by Kim et al. (2002). Its X-ray colour (XMM7 in Fig. 5) and radio spectral index is consistent with a power law spectrum.

ATCA J005425.2–374441 also has a very steep spectral index of –1.8, but its X-ray colour (XMM1) is a bit softer. Still, it is certainly possible that this object also has a X-ray power

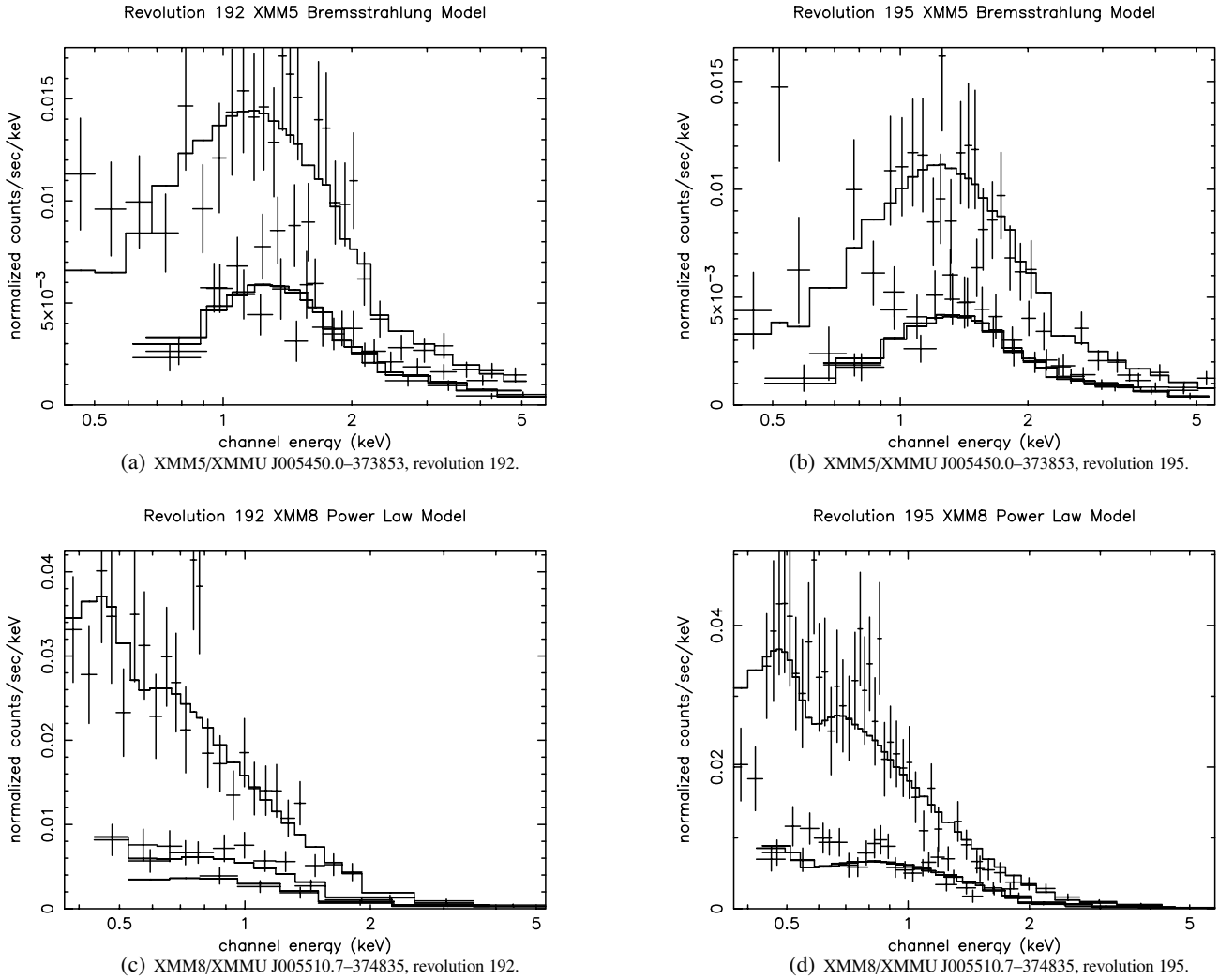

(a) XMM5/XMMU J005450.0–373853, revolution 192.
(b) XMM5/XMMU J005450.0–373853, revolution 195.
(c) XMM8/XMMU J005510.7–374835, revolution 192.
(d) XMM8/XMMU J005510.7–374835, revolution 195.

Fig. 10. Spectrum fits for our *XMM-Newton* sources 5 and 8. In each diagram, grouped spectral data show model fits from PN data (*top*) with MOS 1 and MOS 2 data below (x-axis shows energy range, 0.3 keV to ~6.0 keV; y-axis shows counts per second per keV). The best simple fit for source 5 is the photoelectric absorption bremsstrahlung model while that for source 8 is the photoelectric absorption power law model.

law spectrum as evidenced by its X-ray colour proximity to ATCA J005510.8-374835 (Fig. 9d) which clearly corresponds to an AGN (XMM8) as reported by Read & Pietsch (2001). Using *XMM-Newton* data, we were able to fit a photoelectric absorption power law model to the latter as shown in Figs. 10c and 10d (also see Table 5).

Based on spectral index alone, there are at least two other probable background sources. It is not possible to tell if the remaining 10 "bkg" objects are really background objects as they could represent a different source type.

ATCA J005450.3–373850 (Fig. 9a) is possibly associated with an X-ray binary[2](XMM5) as reported by Read & Pietsch (2001) which they base on its distance of 30″ from the nearest SNR and its HR2 value of 0.75. Using HRI data, they also found a 41% probability that the X-ray source is variable. We have labeled this source "xrb" since the spectrum we found is also consistent with their conclusion. Our X-ray model fit shows the object to have a photoelectric absorption Bremsstrahlung spectrum (Figs. 10a and 10b). However, the photoelectric absorption power law fit is also very good (see XMM5 in Table 5). Perhaps this object has both thermal and power law properties. Its radio emission may be the result of synchrotron emission from jets, making this a rare example of a microquasar. Only one other suspected extragalactic microquasar has been reported by Dubus (2003) (in the nucleus of M 33). We expect this type of source to be rarely found in extragalactic studies since detection of the relatively faint radio emission is unlikely at far distances.

6. Discussion and conclusions

PDL could place only limits on the radio spectral indices from eight of their 14 radio sources because they had only one flux density ($\lambda = 20$ cm) for each of them. One of the goals of the present study is to expand on those observations using new ATCA and *XMM-Newton* data. Our findings do support the six SNRs identifications that they made for radio sources having

[2] X-ray emission from accretion onto a compact star from a normal star in a binary system.

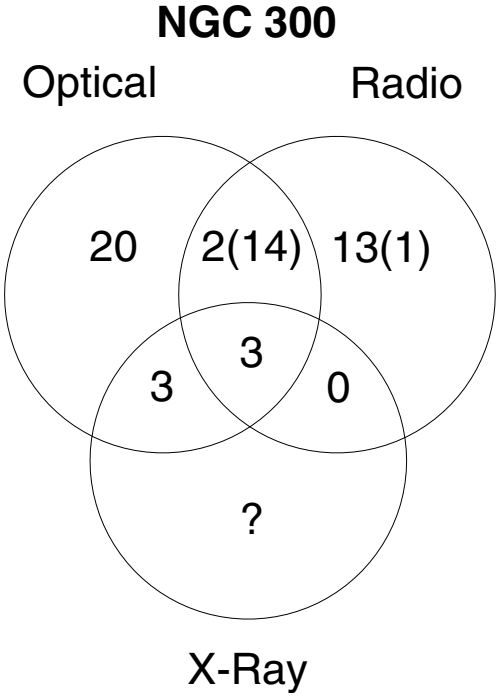

Fig. 11. Venn diagram showing the intersection of selected sets of SNRs for NGC 300. Optical refers to the objects listed in BL97. Parenthesis show the total number of SNRs in each category if our additional [S II] optical identifications are added to those reported by BL97. The "?" denotes that at this time, we do not know the total number of X-ray SNRs within this galaxy. That information is being prepared by S. Carpano for later independent publication.

VLA flux densities at both 6 and 20 cm wavelengths and we pick up a 6 cm flux density for their R1 allowing us to agree with a total of seven of their sources. We also name their R2 as a possible "snr" only, since its association with Read & Pietsch (2001) P44 has been called into doubt by those authors (see page 980 of Pannuti et al. 2002). While we disagree with six of PDL's SNRs, with the addition of ATCA flux densities in the 13 and 20 cm wavelength range, we find an additional six radio SNRs. Updating Fig. 9 in Pannuti et al. (2002) we present a Venn diagram depicting the intersection of sets of SNRs within NGC 300 in Fig. 11. The diagrams are very similar except that we do not include "possible" X-ray sources and although the number of radio sources is almost identical, they do not represent the same sources between the two studies. The optical and radio numbers in parentheses represent the number of SNRs in these categories if our additional BL97 identifications with radio sources are included.

In summary, out of a total of 54 radio sources, we have found and described 18 SNRs in NGC 300; 13 in addition to those found in the optical by BL97. Three of the five SNRs identified by BL97 that have radio counterparts also have X-ray counterparts. We find evidence for [S II] emission from an additional 12 of our radio sources, implying that a total of 17 SNRs have some optical component.

There are three additional SNR candidates in NGC 300 which will await further studies for verification. These sources do not appear to have any optical component, although ATCA J005528.2–374903 is not within the boundary of the BL97 images.

All identifications with *ROSAT* sources are included in our *XMM-Newton* X-ray identifications with radio sources except source number 2 (coincident with PDL's R2 discussed above) reported in Read et al. (1997). Although this source could be a supernova remnant also, we do not have a radio spectral index to prove it.

We have investigated the luminosity functions of our SNRs and find that conclusions about them as a group cannot be made since we are selecting for only the most luminous SNRs.

While it has been understood that many SNRs lie embedded within H II regions, we also note a strong correlation of our radio sources with OB associations within this galaxy. This is another good place to look for SNRs from massive progenitor stars.

We also find the expected number of background sources within the region covered by NGC 300. We note that other objects, for example, globular clusters near NGC 300, may lie in the same direction, thus adding some confusion with identification of sources. An additional seven *XMM-Newton* X-ray sources match our radio sources other than the SNRs mentioned above. Three are identified with background objects and one is associated with a likely X-ray binary as discussed above. Also, two X-ray sources could be background objects while one identifies with another X-ray supernova candidate (P36) discussed in Read & Pietsch (2001). The latter's counterpart, XMM10, shows hardness ratios consistent with a thermal spectrum but we have no additional information to prove it as a SNR.

Acknowledgements. We thank Wolfgang Pietsch and Andy Reid for allowing us to use their *ROSAT* image of NGC 300 for our analysis. T.G.P. would like to thank the staff of the ATNF for their hospitality during the observing run. We also used the Karma software package developed by the ATNF and the EXSAS/MIDAS software package developed by the MPE. E. M. Berkhuijsen deserves thanks for her advice and kind patience.
We also thank William Blair who graciously provided us with the images of NGC 300 used in BL97. These Los Campanas Observatory observations were transferred from tape at our request.
DSS2-Red (R) plates were based on photographic data obtained using the UK Schmidt Telescope. The UK Schmidt Telescope was operated by the Royal Observatory Edinburgh, with funding from the UK Science and Engineering Research Council, until 1988 June, and thereafter by the Anglo-Australian Observatory. Original plate material is copyright (c) of the Royal Observatory Edinburgh and the Anglo-Australian Observatory. The plates were processed into the present compressed digital form with their permission. The Digitized Sky Survey was produced at the Space Telescope Science Institute (STScI) under US Government grant NAG W-2166. TGP gratefully acknowledges support from a Chandra General Observer Award issued by the Smithsonian Astrophysical Observatory.

References

Blair, W. P., & Long, K. S. 1997, ApJS, 108, 261 (BL97)
Braun, R., & Walterbos, R. A. M. 1993, A&AS, 98, 327
Chen, C. H. R., & Chu, Y.-H. 1998, AAS, 193, 7405C
Deharveng, L., Caplan, J., Lequenx, J., et al. 1988, A&AS, 73, 407

Dyer, K. K., & Reynolds, S. P. 1999, ApJ, 526, 365
Dubus, G. 2003, in Semaine de l'Astrophysique Française, ed. F. Combes, D. Barret, & T. Contini (EDP-Sciences), 202
Dunne, B. C., Points, S. C., & Chu, Y. 2001, ApJS, 136, 119
Ehle, M., et al. 2003, *XMM-Newton* Users' Handbook, free online at http://xmm.vilspa.esa.es/
Filipović, M. D., Haynes, R. F., White, G. L., & Jones, P. A. 1998, A&AS, 130, 421
Freedman, W. L., Madore, B. F., Gibson, B. K., et al. 2001, ApJ, 553, 47F
Gooch, R. 1996, ADASS, 5, 80
Gordon, S. M., Kirschner, R. P., Long, K. S., et al. 1998, ApJS, 117, 89
Gordon, S. M., Duric, N., Kirshner, R. P., Goss, W. M., & Viallefond, F. 1999, ApJS, 120, 247
Greisen, E. W. 2003, AIPS, the VLA and the VLBA, in Information Handling in Astronomy – Historical Vistas, ed. A. Heck (Dordrecht: Kluwer Academic Publishers), ISBN 1-4040-1178-4, Astrophysics and Space Science Library, 285, 109
Haberl, F., Filipović, M. D., Pietsch, W., & Kahabka, P. 2000, A&AS, 142, 41
Kim, S. C., Sung, H., & Lee, M. G. 2002, JKAS, 35, 9
Kong, A. K. H., & Di Stefano, R. 2003, ApJ, 590, L13
Koyama, K., Kinugasa, K., Matsuzaki, K., et al. 1997, PASJ, 49L, 7K
Lacey, C. K., & Duric, N. 2001, ApJ, 560, 719
Loiseau, N. 2003, Users' Guide to the *XMM-Newton* Science Analysis System, free online at http://xmm.vilspar.esa.es/
Mitchell, K. J., & Condon, J. J. 1985, AJ, 90, 1957
McGee, R. X., & Newton, L. M. 1972, Aust. J. Phys., 25, 619
Pannuti, T. G., Duric, N., Lacey, C. K., et al. 2000, ApJ, 544, 780
Pannuti, T. G., Duric, N., Lacey, C. K., et al. 2002, ApJ, 565, 966
Pietrzyński, G., Gieren, W., Fouqué, P., & Pont, F. 2001, A&A, 371, 497
Read, A. M., & Pietsch, W. 2001, A&A, 373, 473
Read, A. M., Ponman, T. J., & Strickland, D. K. 1997, MNRAS, 286, 626
Sault, B., & Killeen, N. 2003, MIRIAD users Guide, ATNF
Soffner, T., Meńdez, R. H., Jacoby, G. H., et al. 1996, A&A, 306, 9S
Tully, R. 1988, Nearby Galaxies Catalog (Cambridge: Cambridge University Press)
Trümper, J. 1982, Adv. Space Res., 2, 241
Williams, R. M., Chu, Y.-H., Dickel, J. R., et al. 1999, ApJS, 123, 467

Online Material

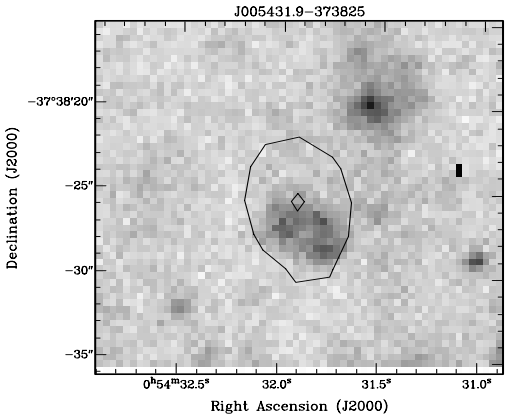

(a) ATCA J005431.9–373825 at 1374 MHz. (BL-S6)

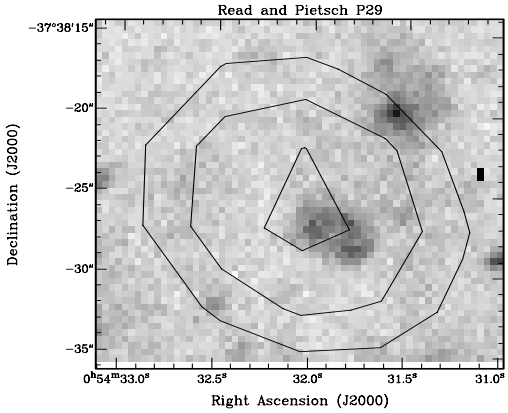

(b) *ROSAT* (P29) image contours: 2.2, 2.3 and 2.4 in units of 10^{-3} cnts s^{-1} $arcmin^{-2}$.

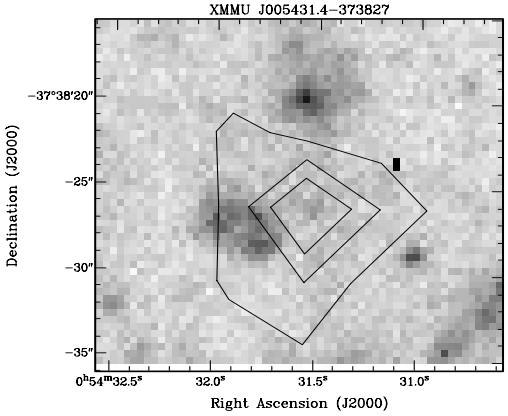

(c) *XMM-Newton* (XMM2) image contours: 2.7, 4.1 and 5.5 in units of 10^{-2} cnts s^{-1} $arcmin^{-2}$.

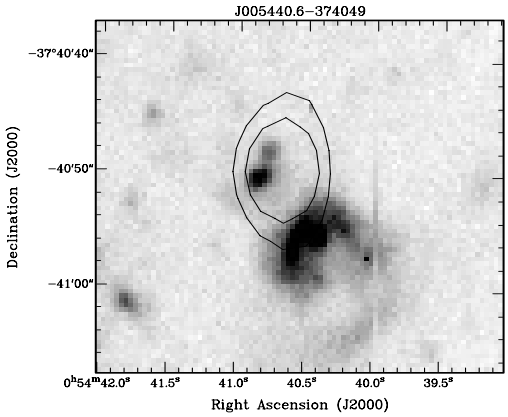

(d) ATCA J005440.6–374049 at 1374 MHz. (BL-S10)

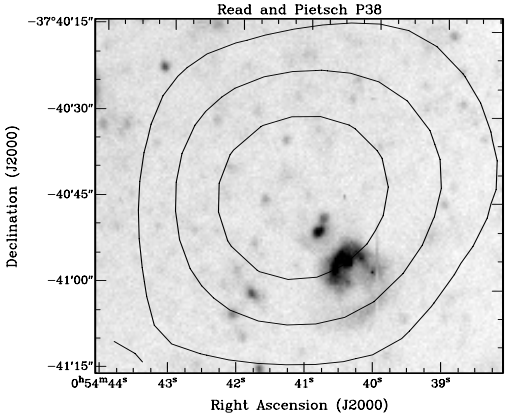

(e) *ROSAT* (P38) image contours: 2.0, 2.7 and 3.8 in units of 10^{-3} cnts s^{-1} $arcmin^{-2}$.

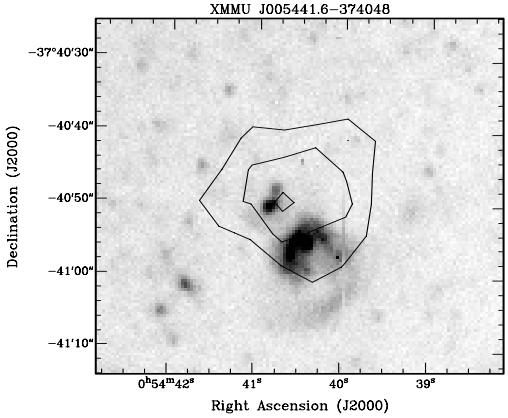

(f) *XMM-Newton* (XMM3) image contours: 4.1, 8.2 and 16.5 in units of 10^{-2} cnts s^{-1} $arcmin^{-2}$.

Fig. 8. SNRs with radio and X-ray contours in NGC 300 overlaying BL97 1500s [S II] images. Radio contours are ∼3 and 5 sigma values (0.174 and 0.291 mJy $beam^{-1}$ for 1374 MHz; 0.198 and 0.330 mJy $beam^{-1}$ for 1448 MHz; 0.186 and 0.311 mJy $beam^{-1}$ for 2496 MHz).

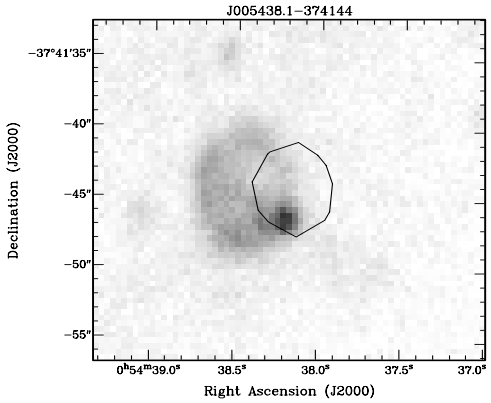

(g) ATCA J005438.1–374144 at 1374 MHz.

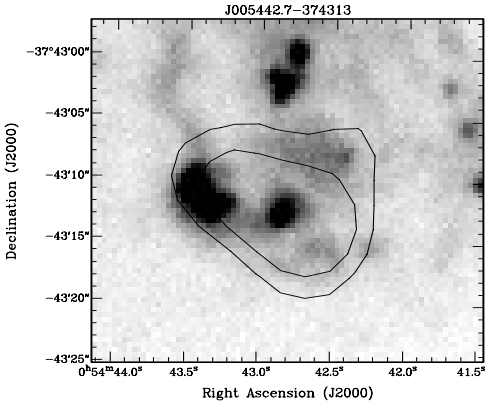

(h) ATCA J005442.7–374313 at 1448 MHz. (BL-S11)

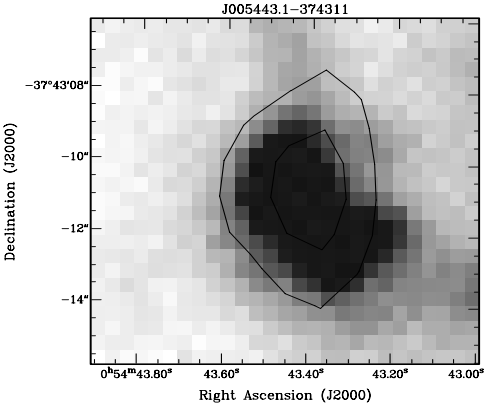

(i) ATCA J005443.1–374311 at 1448 MHz.

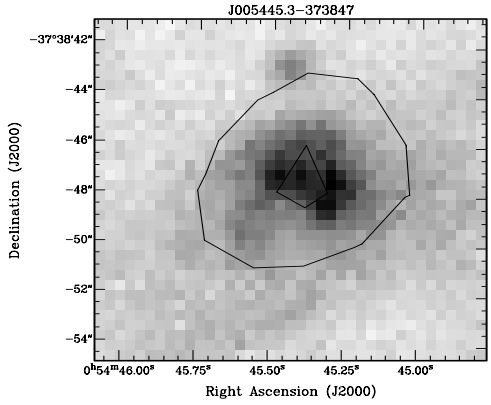

(j) ATCA J005445.3–373847 at 1374 MHz.

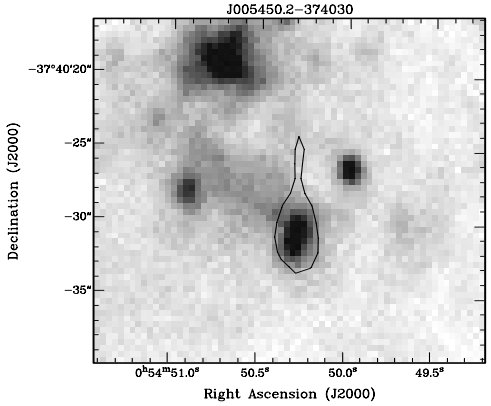

(k) ATCA J005450.2–374030 at 1448 MHz.

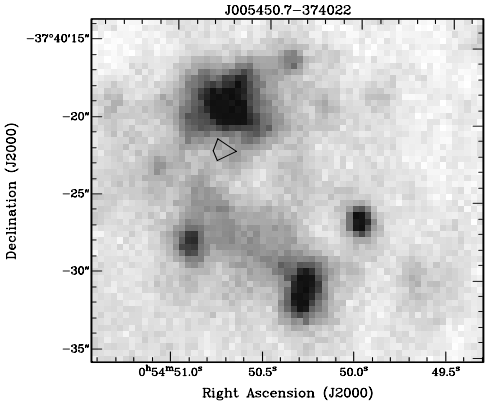

(l) ATCA J005450.7–374022 at 1374 MHz.

Fig. 8. continued.

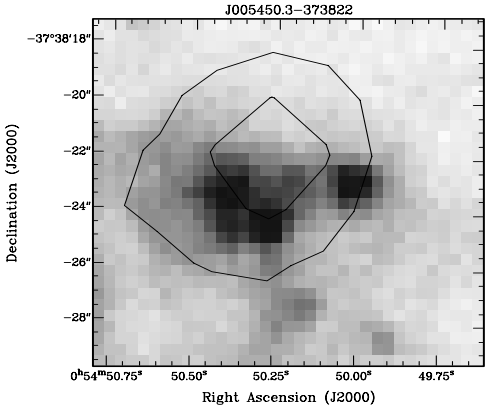

(m) ATCA J005450.3–373822 at 1374 MHz.

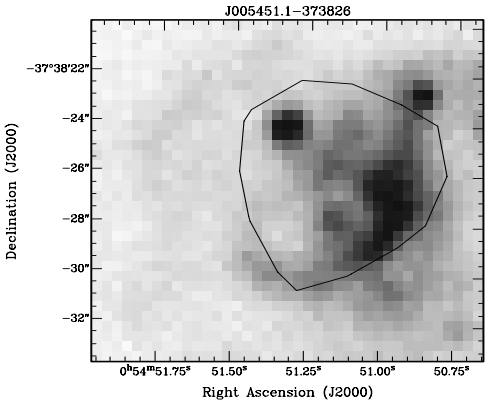

(n) ATCA J005451.1–373826 at 1374 MHz.

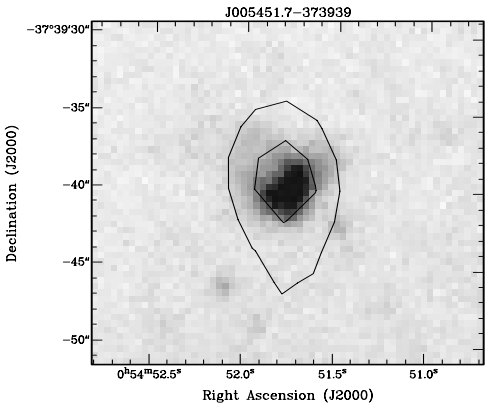

(o) ATCA J005451.7–373939 at 1374 MHz.

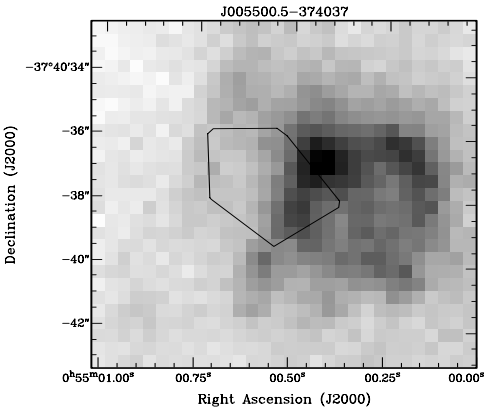

(p) ATCA J005500.5–374037 at 1374 MHz.

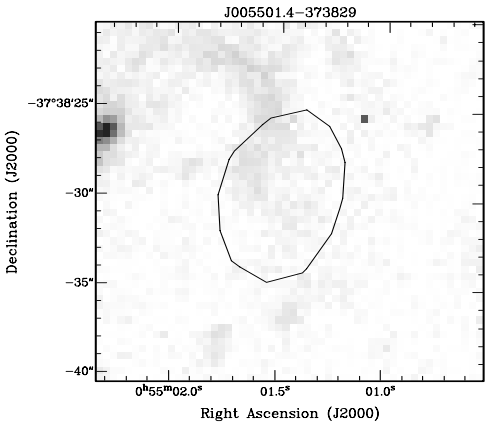

(q) ATCA J005501.4–373829 at 1374 MHz.

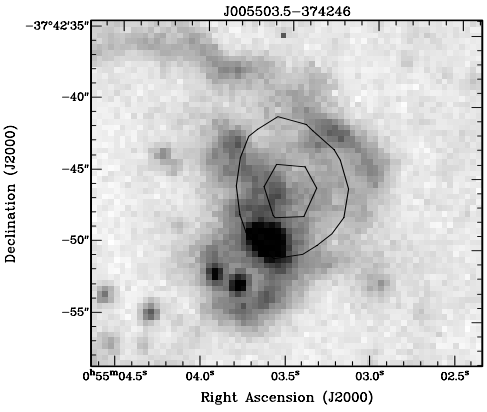

(r) ATCA J005503.5–374246 at 1374 MHz.

Fig. 8. continued.

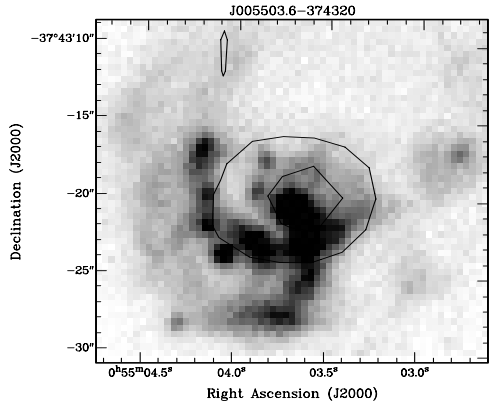

(s) ATCA J005503.6–374320 at 1374 MHz.

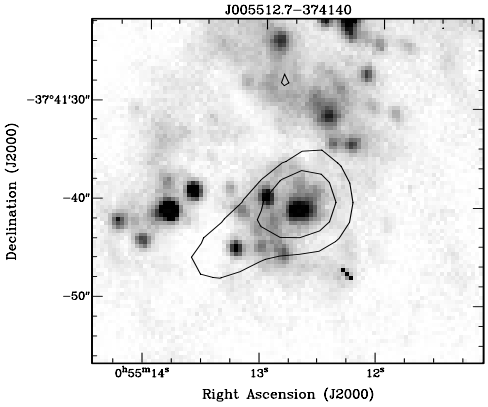

(t) ATCA J005512.7–374140 at 1374 MHz.

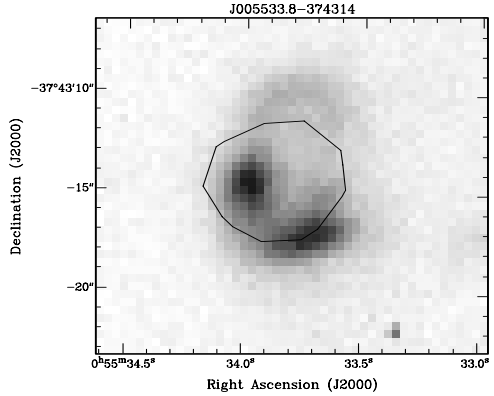

(u) ATCA J005533.8–374314 at 1374 MHz. (BL-S28)

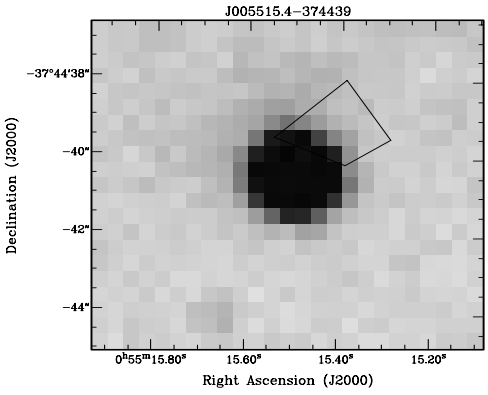

(v) ATCA J005515.4–374439 at 1374 MHz. (BL-S26)

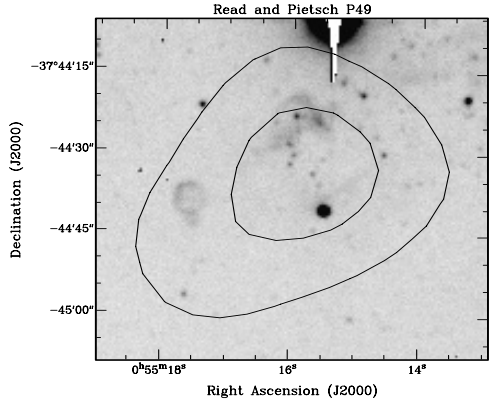

(w) *ROSAT* (P49) image contours: 2.0 and 2.7 in units of 10^{-3} cnts s^{-1} $arcmin^{-2}$.

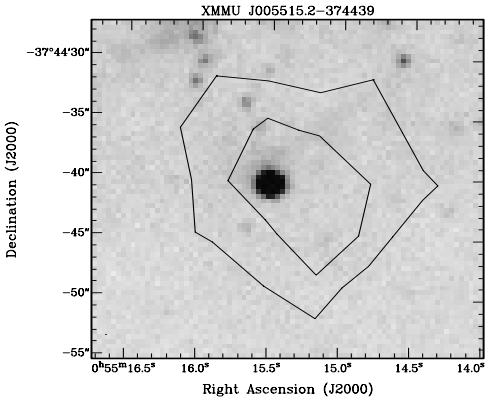

(x) *XMM-Newton* (XMM9) image contours: 2.7 and 5.5 in units of 10^{-2} cnts s^{-1} $arcmin^{-2}$.

Fig. 8. continued.

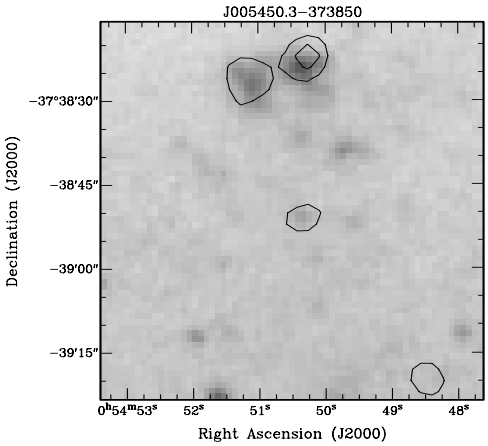

(a) ATCA J005450.3–373850 at 1374 MHz. (X-ray binary)

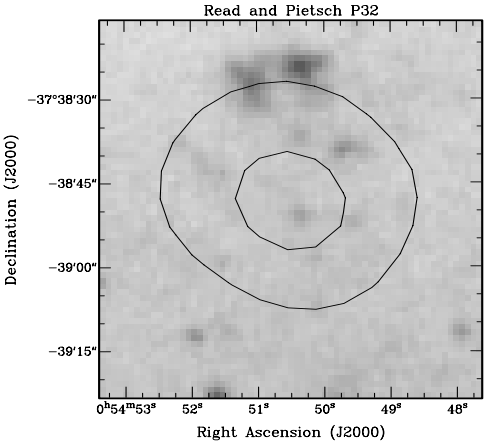

(b) *ROSAT* (P32) image contours: 2.0 and 2.7 in units of 10^{-3} cnts s^{-1} $arcmin^{-2}$.

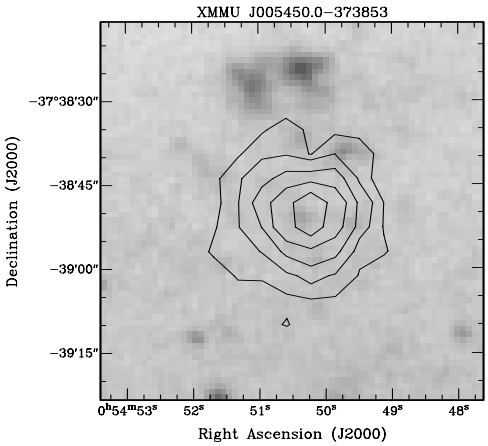

(c) *XMM-Newton* (XMM5) image contours: 4.1, 8.2, 16.5, 32.9 and 65.9 in units of 10^{-2} cnts s^{-1} $arcmin^{-2}$.

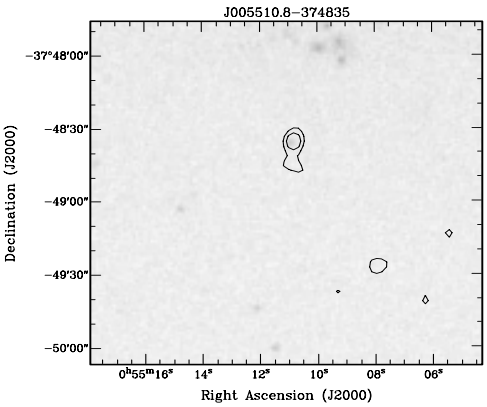

(d) ATCA J005510.8–374835 at 1374 MHz. (AGN)

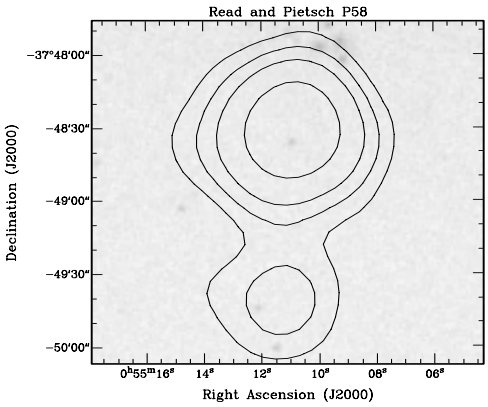

(e) *ROSAT* (P58) image contours: 2.0, 2.7, 3.8 and 6.9 in units of 10^{-3} cnts s^{-1} $arcmin^{-2}$.

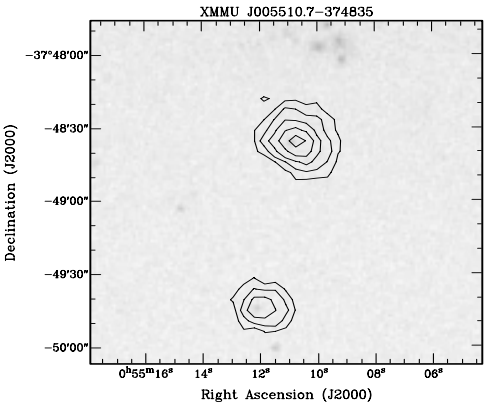

(f) *XMM-Newton* (XMM8) image contours: 4.1, 8.2, 16.5, 32.9 and 65.9 in units of 10^{-2} cnts s^{-1} $arcmin^{-2}$.

Fig. 9. Other interesting objects in NGC 300 with radio and X-ray contours overlaying the DSS2-Red (*R*) image. 1374 MHz contours are 0.174 and 0.291 mJy $beam^{-1}$.